



저작자표시-비영리-변경금지 2.0 대한민국

이용자는 아래의 조건을 따르는 경우에 한하여 자유롭게

- 이 저작물을 복제, 배포, 전송, 전시, 공연 및 방송할 수 있습니다.

다음과 같은 조건을 따라야 합니다:



저작자표시. 귀하는 원 저작자를 표시하여야 합니다.



비영리. 귀하는 이 저작물을 영리 목적으로 이용할 수 없습니다.



변경금지. 귀하는 이 저작물을 개작, 변형 또는 가공할 수 없습니다.

- 귀하는, 이 저작물의 재이용이나 배포의 경우, 이 저작물에 적용된 이용허락조건을 명확하게 나타내어야 합니다.
- 저작권자로부터 별도의 허가를 받으면 이러한 조건들은 적용되지 않습니다.

저작권법에 따른 이용자의 권리와 책임은 위의 내용에 의하여 영향을 받지 않습니다.

이것은 [이용허락규약\(Legal Code\)](#)을 이해하기 쉽게 요약한 것입니다.

[Disclaimer](#)



공학박사 학위논문

**Analysis of Radio Frequency Induction Plasma Process for
Mass Production of Ni Nanoparticles**

니켈 나노입자의 대량생산을 위한
고주파 유도결합 열플라즈마 공정 해석

2016년 8월

서울대학교 대학원

원자핵공학과

남 준석

Analysis of Radio Frequency Induction Plasma Process for Mass Production of Ni Nanoparticles

**니켈 나노입자의 대량생산을 위한
고주파 유도결합 열플라즈마 공정 해석
지도교수 김 곤 호**

이 논문을 공학박사 학위논문으로 제출함

2016년 4월

**서울대학교 대학원
원자핵공학과
남준석**

남준석의 박사 학위논문을 인준함

2016년 6월

위 원 장	<u>황 용 석</u>	(인)
부위원장	<u>김 곤 호</u>	(인)
위 원	<u>김 응 수</u>	(인)
위 원	<u>서 준 호</u>	(인)
위 원	<u>정 경 재</u>	(인)

Abstract

Analysis of Radio Frequency Induction Plasma Process for Mass Production of Ni Nanoparticles

Jun Seok Nam

Department of Nuclear Engineering
The Graduate School
Seoul National University

As the demand for nickel nanopowders is recently increasing as electrode material of microelectronic devices such as multilayer ceramic capacitors (MLCCs), it is essential for the industrial applications to develop the economical method for the mass production of nickel nanoparticles. Especially, spherical nickel nanoparticles with narrow size distribution are favored for high-tech MLCCs with high performance. However, conventional nanoparticle synthesis routes such as ball milling, sol-gel and spray pyrolysis methods have a limitation in manufacturing nickel nanoparticles which meets the industrial needs. Meanwhile, radio frequency (RF) induction plasmas have attracted much attention as a powerful tool to prepare spherical nanopowders. In spite of the advantages of induction plasma process in the synthesis of spherical nanopowders, the difficulty in scale-up of RF induction plasma systems and the resultant low production rate are frequently mentioned as the weakness in industrial applications. In order to overcome this weakness, a high powered RF induction plasma process for mass production of nickel nanoparticles is studied through the numerical modelling and experiment.

The primary purpose of this dissertation is to develop a practical RF induction plasma process for the mass production (~ 16.7 g/min) of well-

dispersed spherical nickel nanoparticles with high purity and good crystallinity using solid nickel precursor. In order to vaporize the nickel precursor at the high feed rate of ≥ 16.7 g/min, a high-powered RF thermal plasma should be generated and maintained. For the stable operation at high power level of ≥ 50 kW, Ar-N₂ RF-ICP (Radio Frequency Inductively Coupled Plasma) was proposed because Ar only ICP is difficult to scale up the plasma power higher than 30 kW due to the rapid increase of radiation loss. The existence of N₂ in Ar-N₂ induction plasmas is expected to alleviate the radiation loss of the plasma and to improve the thermal conductivity of plasma, which enhances the heat transfer from plasma to the injected precursor and the mass production of Ni nanopowders.

In order to find the power-up process of Ar-N₂ induction plasma higher than 50 kW, thermal flows and the electrical characteristics of Ar-N₂ ICPs were investigated based on the numerical results of 2-dimensional MHD (Magneto-Hydro Dynamic) equations for Ar-N₂ RF-ICP combined with the basic circuit theory. Based on these numerical studies, the optimum N₂ content are presented for Ar-N₂ ICPs with the power level of 50 kW. A simplified PSI-Cell model were developed to consider the plasma-particle interaction with dense loading of raw nickel powders conditions for the mass production of nickel nanoparticles. From the computational study, effects of process parameters on the plasma characteristics and the behaviors of particles injected into the induction torch are investigated.

Firstly, the effects of carrier gas flow on the flow fields of induction plasma and the behavior of a single particle injected into an induction torch are investigated. The introduction of cold carrier gas for powder feeding makes a low temperature zone downstream from the position of powder injection probe tip in the central region of RF induction torch. The low temperature zone expands and elongates with the increase of the carrier gas flow rate. As the

carrier gas flow rate increases, the initial axial velocity of particle loaded in carrier gas flow is increased. As a result, the residence time of particle in high temperature region decreases, which is disadvantageous to particle heat treatment. Therefore, the carrier gas flow rate should be minimized as much as possible for the complete evaporation of the powder injected.

Secondly, the effects of N₂ mole fraction of the plasma gas on the plasma characteristics and the behavior of particles injected into induction torch are studied. The addition of N₂ can reduce down the percentage of radiation power loss. The highest temperature region of ~ 10,000 K is significantly diminished for Ar-N₂ induction plasma with the N₂ mole fraction of 20 %, which is attributed to the increase of specific heat, enthalpy and thermal conductivity for N₂ addition. The Ar-N₂ mixture gas is advantageous to vaporize nickel particles due to the enhanced plasma-particle interaction.

Thirdly, the effects of nickel feed rate on the temperature field of induction plasma and the behavior of particles injected into an induction torch are investigated. As the nickel feed rate increases, the plasma temperature drop near the particle trajectories increases due to the plasma-particle interaction. When the plasma is cooled down below the boiling point of nickel, plasma-particle heat transfer is reduced and the complete vaporization of the injected particles is difficult. The particles moving along with the outer trajectories far away from the symmetric axis of the torch can be completely vaporized because they pass through the high temperature region of induction plasma. However, the particles moving along with the inner trajectories close to the centerline of the torch can be partly vaporized because they pass through the low temperature region of induction plasma.

Fourthly, the increase of RF power input affects two opposing effects. On the one hand, the increase of RF power input raises the plasma temperature, which has the favorable effects on the vaporization of the particles. On the other

hand, the rise of RF power input increases the plasma axial velocity, which is disadvantageous to the vaporization of the particles. Consequently, the optimal RF power input to evaporate nickel powders is expected to exist.

In order to demonstrate the feasibility of the RF induction plasma process for the mass production of nickel nanoparticles, the RF induction plasma system for the preparation of nickel nanoparticles was constructed and the experimental work was carried out based on the computational study. Well-dispersed spherical nickel nanoparticles are successfully produced at an RF power input of 50 kW, 20 mol % of N₂ and a nickel feed rate of 20 g/min with the production yield of 65 wt. %. The mass production of Ni nanoparticles with spherical shape, high dispersion, high crystallinity and high purity is achieved via RF induction plasma process.

Keywords: Radio Frequency (RF) induction plasma, inductively coupled plasma, plasma-particle interaction, synthesis of nanoparticles, nickel, modeling

Student Number: 2004-30210

Table of Contents

Abstract	i
Table of Contents	v
List of Figures	vii
List of Tables	xii
List of Terms	xii
Nomenclature	xiii
Chapter 1. Introduction	1
1.1. Background	1
1.2. Various methods for the preparation of nanoparticles.....	4
1.3. Induction plasma.....	6
1.4. Objectives and scope of the present work.....	8
Chapter 2. Numerical model	13
2.1. Computational domain and basic assumptions for RF-ICP simulation.....	13
2.2. Properties of thermal plasmas	16
2.3. Governing equations for RF-ICP	18
2.4. Boundary conditions for RF-ICP.....	20
2.5. Equivalent circuit and electrical parameter calculation	22
2.6. Plasma-particle interactions: Particle trajectory and temperature history.....	27
2.7. Plasma-particle interactions: Particle Source In Cell (PSI-Cell) Model.....	30

Chapter 3. Numerical analysis of electrical and thermal flow characteristics of Ar-N ₂ inductively coupled thermal plasmas	35
3.1. Effect of N ₂ addition on thermal flow characteristics of RF-ICP.	35
3.2. Effect of N ₂ addition on electrical characteristics of RF-ICP.....	40
Chapter 4. Simulations on RF induction plasma characteristics and the particle behavior injected into the plasma	45
4.1. Effect of carrier gas flow rate	45
4.2. Effect of N ₂ addition	49
4.3. Effect of Ni feed rate	52
4.4. Effect of RF Power.....	56
Chapter 5. Experiments on mass production of Ni nanoparticles by RF thermal plasma process	60
5.1. Experimental setup and material characterization	60
5.2. Mass production of nickel nanoparticles by RF thermal plasma process	68
Chapter 6. Conclusions	76
 References	79
Appendix	86
초록	90

List of Figures

Figure 1. 1 A photograph of Multi-Layer Ceramic Capacitors.....	1
Figure 1. 2 A cross-sectional view of a multilayer ceramic capacitor.....	2
Figure 1. 3 A schematic of a ball mill.....	5
Figure 1. 4 A schematic of objectives and approach of the present work...	11
Figure 2. 1 Schematic of RF induction torch.....	14
Figure 2. 2 A cross sectional view of the induction coil segments and plasma cells.	23
Figure 2. 3 Electrical circuit of RF ICP.....	26
Figure 2. 4 Equivalent circuit of RF ICP.	26
Figure 2. 5 Flow chart of simulation.	34
Figure 3. 1 (a) Radiation power losses and (b) exit enthalpies calculated for N2 mole fractions from 0% to 50% at RF power level of 50 kW.	36
Figure 3. 2 Comparison of temperature contours between (a) Ar only and (b) Ar-N2 RF-ICPs calculated at plasma power level of 50 kW. For Ar- N2 RF-ICP, N2 content is 20 mol %.	38
Figure 3. 3 Comparison of Radial distributions of (a) temperatures and (b) velocities at torch exit plane calculated for Ar only and Ar-N2 RF- ICPs. For Ar-N2 RF-ICP, N2 content is 20 mol %.	39

Figure 3. 4 (a) Equivalent plasma resistance and (b) equivalent plasma inductance calculated for N ₂ mole fractions from 0% to 50% at RF power level of 50 kW.....	41
Figure 3. 5 Coil currents calculated for N ₂ mole fractions from 0% to 50% at power level of 50 kW	42
Figure 3. 6 Coupling efficiencies calculated for N ₂ contents from 0 mol % to 50 mol % at power level of 50 kW.....	42
Figure 3. 7 Resonance tank circuit consisting of a capacitor in parallel connection with an equivalent resistance and an equivalent inductance of an RF-ICP	44
Figure 4. 1 Temperature fields of Ar RF-ICPS at carrier gas flow rates of (a) Q ₁ = 0 slpm, (b) Q ₁ = 3 slpm and (c) Q ₁ = 4 slpm.....	46
Figure 4. 2 Comparison between temperature fields of Ar RF-ICPs at carrier gas flow rates of Q ₁ = 4 slpm (upper part) and (c) Q ₁ = 3 slpm (lower part) for induction coil turn number of 4	47
Figure 4. 3 Trajectories and temperature histories of precursor Ni particle with diameters of 1, 5, 10 and 20 μm at carrier gas flow rates of Q ₁ = 4 slpm (left part) and Q ₁ = 3 slpm (right part).	48
Figure 4. 4 Changes in size and temperature histories of precursor Ni particles starting at different radial points for Ar only (left part) and Ar-N ₂ (right part) RF-ICPs with the power level of 50 kW...50	
Figure 4. 5 Changes in size and temperature histories of precursor Ni particles starting at different radial points for Ar-N ₂ RF-ICPs with N ₂ content of 10 mol % (left part) and 20 mol % (right part) with the power level of 50 kW.....	51

Figure 4. 6 Temperature fields simulated at the RF input power of 50 kW for Ni feed rates of 0.0 g/min (bottom) and 1.0 g/min (top).	53
Figure 4. 7 Temperature fields simulated at the RF input power of 50 kW for Ni feed rates of 0.0 g/min (bottom) and 10.0 g/min (top).....	53
Figure 4. 8 Changes in Ni sizes calculated along six different trajectories in the Ar(80%) - N ₂ (20%) RF-ICP at the power level of 50 kW for Ni feeding rates of (a) 10.0 g/min, (b) 20.0 g/min and (c) 40.0 g/min.	54
Figure 4. 9 The evaporation ratio of the axially injected particles according to the Ni feed rate at the same power level of 50 kW	55
Figure 4. 10 Distributions of temperatures (a) and axial velocities (b) along the centerline according to the various RF input powers without injection of Ni precursor.....	57
Figure 4. 11 Distributions of temperatures (a) and axial velocities (b) at the torch exit plane according to the various RF input powers without injection of Ni precursor.....	58
Figure 4. 12 Evaporation ratio of Ni powder injected at the feed rate of 20 g/min for various RF input powers.....	59
Figure 5. 1 SEM imag Comparison between temperature fields of Ar RF-ICPs at carrier gas flow rates of Q1 = 4 slpm (upper part) and (c) Q1 = 3 slpm (lower part) for induction coil turn number of 4e of nickel raw powders.....	69
Figure 5. 2 SEM images of as-prepared nickel powders collected from cyclone: (a) particles agglomerated in liquid phase, (b) raw powders which did not react with high temperature plasma flume.	71

Figure 5. 3 SEM image of as-prepared nickel nanoparticles collected from filter	69
Figure 5. 4 Particle size distribution calculated from a SEM image.....	70
Figure 5. 5 XRD patterns of raw nickel powders and as-prepared nickel nanoparticles	73
Figure 5. 6 TGA curves of nickel raw powder and as-prepared nickel nanoparticles collected from filter.....	74

List of Tables

Table 1. 1 Comparison of various methods for nanoparticle preparation	3
Table 2. 1 Principal design and operation parameters for ICP torch	15
Table 2. 2 Boundary conditions for RF-ICP.....	21
Table 2. 3 Physical Properties of Nickel [29].....	33
Table 5. 1 Specification of a self-excited type RF power supply with vacuum tube.....	64
Table 5. 2 Principal design parameters and the operating conditions of RF induction plasma system for synthesis of Ni nanoparticles	66

List of Terms

DC	Direct Current
FE-SEM	Field Emission – Scanning Electron Microscopy
ICP	Inductively Coupled Plasma
LTE	Local Thermodynamic Equilibrium
MHD	Magneto Hydro Dynamics
MLCC	Multi-Layer Ceramic Capacitor
PSI-Cell	Particle Source In – Cell
RF	Radio-Frequency
SEM	Scanning Electron Microscopy
TGA	Thermo-Gravimetric Analysis
XRD	X-Ray Diffraction

Nomenclature

A_R	real part of magnetic vector potential
A_I	imaginary part of magnetic vector potential
B	magnetic field intensity
C	particle concentration in a cell
C_D	drag coefficient
c_p	specific heat at constant pressure
D	diffusion coefficient
D_p	particle diameter
E_θ	circumferential electric field intensity
F_r	body force in the radial direction
F_z	body force in the axial direction
g	acceleration of gravity
H_m	latent heat of melting
H_r	radial magnetic field intensity
H_v	latent heat of evaporation
H_z	axial magnetic field intensity

h	enthalpy
h_c	convective heat transfer coefficient
J	current density
k	thermal conductivity
\dot{m}_p	powder feed rate
Δm_p	change in the mass of the particle
N_t	total number of particles injected per unit time
n_d	fraction of N_t used in the discretized particle diameter distribution
n_r	fraction of N_t injected at each point
Nu	Nusselt number
p	Pressure
P_0	plasma power
Q_1	carrier gas flow rate
Q_2	central gas flow rate
Q_3	sheath gas flow rate
Q_r	radiation loss energy
R_0	inner radius of the plasma confinement tube

R_1	inner radius of the particle injector
R_c	radius of coil turn
r	distance in the radial distance
Re	Reynolds number
S_p^c	particle source term in the continuity equation
$S_p^{M_r}$	particle source term in the radial momentum equation
$S_p^{M_z}$	particle source term in the axial momentum equation
S_p^E	particle source term in the energy equation
T	temperature
t	time
u	axial velocity component
U_R	relative speed of a particle with respect to plasma gas
v	radial velocity component
x	liquid fraction of a particle
z	distance in the axial direction

Greek symbols

μ	viscosity
-------	-----------

ρ	density
σ	electrical conductivity
τ	residence time of a particle in a cell

Subscripts

p	particles
l	particles with initial diameter of D_l
k	particles injected at radius r_k

Superscripts

(l, k)	particles with an initial diameter D_l and injection point r_k
----------	--

Chapter 1. Introduction

1.1. Background

Nickel powders have attracted great attention due to their important industrial applications, such as conductive paste^{[1], [2]}, chemical catalyst and magnetic material^[3]. Micrometer-sized nickel powders already began to be manufactured by carbonyl process in the late 1800s^[4]. With the development of portable electronic machines (for example, mobile phone, notebook, tablet, and so forth), the demand for nickel nano-powders is recently increasing as internal electrode material of microelectronic devices such as multilayer ceramic capacitor (MLCC) as shown in Fig. 1.1^{[5], [6]}. Moreover, state-of-the-art technology for high performance MLCCs requires that the average size of nickel nano-powders should be controlled smaller than 100 nm.



Figure 1. 1 A photograph of Multi-Layer Ceramic Capacitors.

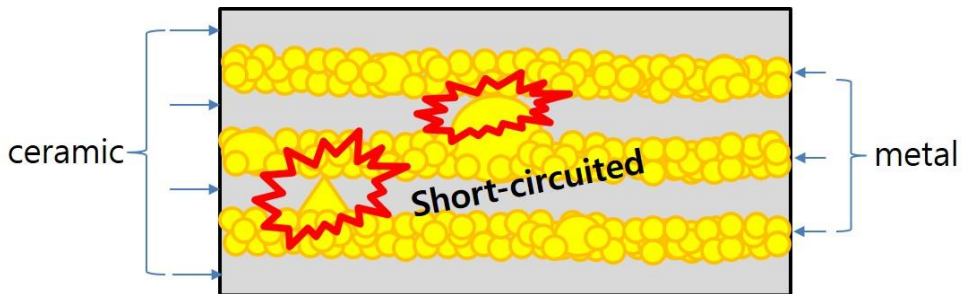


Figure 1. 2 A cross-sectional view of a multilayer ceramic capacitor.

In addition, nickel nano-powders are preferred to be prepared in spherical shape with a narrow size distribution for their easy dispersion during MLCC fabrication process and for minimizing the failure by making a short circuit between inner electrode layers as described in Fig. 1.2.

Various methods have been reported for the preparation of nickel nanoparticles: ball milling^[7], sol-gel^{[8], [9]}, polyol^[10], chemical reduction^[11], hydrothermal^[12], laser ablation^[13], microwave plasma^[14] and spray pyrolysis^[15] methods. However, these conventional methods have some problems and limitations in the mass production of nickel nanoparticles which meet the above-mentioned requirements^[16]. For example, ball milling method has some disadvantages over alternative techniques such as the contamination from milling medium, the irregular shape of the crushed powders and the ineffective milling efficiency at sub-micrometer range^{[17], [18]}. Wet chemical routes such as sol-gel and chemical reduction also suffer from the drawback of the particle agglomeration due to washing, drying and heat-treatment. Consequently, it is required to develop the economical method for manufacturing spherical nickel nanoparticles with narrow size distribution.

Table 1.1 shows an overall comparison among various methods for the preparation of nanoparticle.

Table 1. 1 Comparison of various methods for nanoparticle preparation

	Advantages	Disadvantages
Ball milling	Simple process	Powder contamination
	Low cost	Irregular shape
		Poor crystallinity
Laser ablation	High purity	Low production rate
	Controllable particle quality	High energy consumption
		High cost
Wet chemical route	Uniform composition	Poor crystallinity
	Narrow size distribution	Highly agglomerated
		Non-spherical shape
Induction plasma	High purity	High energy consumption
	Spherical shape	Low production yield
	Softly agglomerated	
	High flexibility	

1.2. Various methods for the preparation of nanoparticles

(1) Ball milling method

Ball milling is basically a solid state processing technique for the preparation of fine particles. Before a mechanical milling is started, raw powders of micron size are loaded together with a suitable milling medium (steel or tungsten carbide) in a container. By vigorously shaking or rotating the milling chamber, a high mechanical energy is transferred to the powders through collisions between powders and heavy balls. Raw powders are then broken into smaller ones as illustrated in Fig. 1.3. The quality of the final product is affected by many parameters such as the type of mill, the power supplied to drive the milling chamber, milling speed, size and size distribution of the balls, dry or wet milling, atmosphere, temperature of milling and the duration of milling.

Simple operation, low cost and ease of scale-up for mass production are the main advantages of mechanical milling. However, it is very difficult to produce nanoparticles using this technique due to mechanical limitations. Ball attrition by collision can also lead to powder contamination. Moreover, the irregular shape of the crushed powders may aggravate the problems associated with the porosity in the powder sintering.

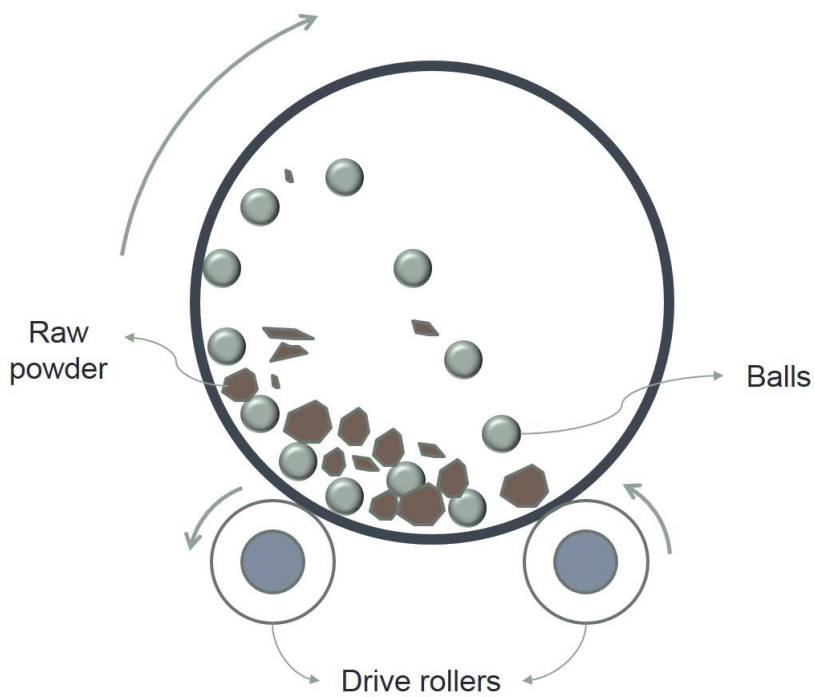


Figure 1. 3 A schematic of a ball mill

(2) Sol-gel method

Sol-gel is a useful technique for the production of nanomaterials made of particles in an insulating matrix with interesting magnetic or optical properties. The sol-gel method is based on inorganic polymerization reaction including hydrolysis, polycondensation, drying, and thermal decomposition. This method has been successfully used to synthesize numerous metal oxide nanoparticles and other nanomaterials. However, the main disadvantages of solution processing such as sol-gel and solution reduction lie in that the direct products are frequently amorphous or low crystalline in nature, which necessitates

additional heat treatments for improvements. This, in turn, inevitably causes a significant aggregation of the initially extremely fine particles.

(3) Laser ablation/ pyrolysis

Laser ablation method is a commonly used technique for the preparation of metal nanoparticles in colloidal form in various solvents to avoid oxidation. The pulse laser ablation process takes place in a vacuum chamber and in the presence of some background/ inert gas. In this method, a high-power pulsed laser beam is focused inside a vacuum chamber to strike a target in the material and plasma is created, which is then converted into a colloidal solution of nanoparticles. Laser pyrolysis is based on the resonant interaction between laser photons and at least one gaseous species, reactants or sensitizer. A sensitizer is an energy transfer agent that is excited by the absorption of the laser radiation and transfers the absorbed energy towards the reactants by collision. The laser-induced pyrolysis offers the advantages of being a potentially clean process producing particles with uniform and controllable size distribution. Particle size is controlled by changing the flow rate of chemicals through the pyrolysis reaction zone. Moreover, the use of laser and a continuous flow reactor is, in principle, scalable to pilot plant dimensions. These methods are very expensive and energy-consuming.

1.3. Induction plasma

The plasma is frequently referred to as the fourth state of matter or the ionized gas which is comprised of electrons, ions, and neutral species in local electrical neutrality. In contrast to an ordinary gas, the free electric charges in

plasma bring about its relatively high electrical conductivity. In general, plasmas are generated by applying the electrical energy to gas. On the other hand, thermal plasmas are characterized by the equality between the electron temperature and the temperatures of heavy particles due to frequent collisions between them under the pressures close to 1 atm. Typical examples of thermal plasmas include those produced by DC (Direct Current) plasma torches or RF (Radio Frequency) induction plasma torches.

In recent decades, RF induction thermal plasmas have been widely employed as a powerful tool to prepare a variety of ultrafine powders [19], [20]: iron [21], fullerenes [22], TiO₂ [23], glass [24], carbon nanotubes [25], indium zinc tin oxide [26]. Normally, RF thermal plasma system can produce a high temperature flame (up to 10,000 K) with a rapidly cooled tail (10^5 – 10^6 K/s) [19]. It can provide not only enough energy for the melting/evaporation of the raw materials but also the quenching region at flame tail, which helps rapid solidification of the melted droplets or condensation of vapor. As a result, spherical powders can be easily prepared from both of melting–spheroidization and evaporation–condensation processes by RF thermal plasma system. For example, melting–spheroidization can be applied in the preparation of micron spheres while evaporation–condensation processes can lead to synthesis routes of spherical nanoparticles. If the particle sizes of the precursor materials are small enough and the feed rate is proper, the precursor materials injected into RF thermal plasma would be fully evaporated and reformed into spherical nanoparticles in the quenching region. In addition, the purity of the as-prepared particles is also improved since RF thermal plasma torch has no contamination source, such as electrodes for sustaining plasma.

Based on the above advantages of RF thermal plasma system, Bai et al. [27] reported successful synthesis of nickel nano-powders via an RF thermal plasma

process. In this work, they used nickel hydroxide or nickel carbonate as a precursor. However, crucial drawbacks were found in this process, such as complex chemical reactions between plasma and precursor and the occurrence of water vapors as a byproduct in exhausting gas. In particular, the condensed water tends to react with the surface of the as-prepared nickel particle, causing agglomeration of nickel particles. Compared with the direct evaporation of solid nickel precursor, additionally, this process may show relatively low production efficiency because the precursors, NiCO_3 and Ni(OH)_2 have low nickel contents of 49.5 wt. % and 63.3 wt. %, respectively.

1.4. Objectives and scope of the present work

In spite of the advantages of RF induction plasma process in the synthesis of spherical nano-powders, the difficulty in scale-up of RF thermal plasma systems and the resultant low production rate are frequently mentioned as the weakness in industrial applications. Production rates of $3.3 \sim 5$ g/min have been reported at the RF input power level of < 30 kW in most of papers dealing with the successful synthesis of nano-powders. In order to overcome this weakness, a high powered RF thermal plasma system needs to be developed together with mass production route to nanoparticles. Recently, commercial RF thermal plasma systems with power level of > 50 kW have been introduced^[16] but their industrial applications to nano-powder production are limited due to extremely high price of the systems and the lack of process manuals for mass production of spherical nano-powders. As reported in many other papers^{[28], [29]}, for example, plasma-particle interactions in RF thermal plasmas depends on physical properties of the injected particles as well as plasma characteristics, such as enthalpy, velocity, thermal conductivity and so on. Consequently, mass

production routes can be different by the target materials for the same operation conditions of RF thermal plasma system.

The primary purpose of this dissertation is to develop a practical RF induction thermal plasma process for the mass production (~ 16.7 g/min) of well-dispersed spherical nickel nanoparticles with high purity and good crystallinity using solid nickel precursor. In order to vaporize the nickel precursor at the high feed rate of ≥ 16.7 g/min, a high-powered RF thermal plasma should be also generated and maintained. For this purpose, we proposed Ar-N₂ RF-ICP (Radio Frequency Inductively Coupled Plasma) with the power level of ≥ 50 kW. Normally, argon gas is favorable for easy ignition and stable operation of RF thermal plasma at low power level due to relatively high electrical conductivity compared with other diatomic gases, such as H₂, N₂ and O₂. At high power operation, however, the increased temperatures of Ar plasma bring about rapid increase of radiation power loss, which can cause a crucial damage on the confinement tube of the torch. Consequently, Ar only RF-ICP is difficult to scale up the plasma power higher than 30 kW.

Since the specific enthalpy of N₂ is larger than that of Ar, N₂ addition to pure Ar RF-ICP can help alleviate these problems by reducing the excessive temperature rising and radiation power loss at high power operation. In addition, nitrogen hardly reacts with nickel and can be safely handled without explosion or toxicity problems. The existence of N₂ in Ar-N₂ RF-ICPs can also improve the thermal conductivity of plasma, which expedites the heat transfer from plasma to the injected precursor, and can help the mass production of Ni nano-powders. However, the addition of N₂ affects not only thermal flow characteristics but also electrical characteristics of RF-ICPs. For example, the diminished volume of plasma is accompanied with the lowered coupling efficiency due to the decrease of magnetic flux linkage. Moreover, electrical conductivity is also decreased. Accordingly, the electrical power transfer from

RF power supply to plasma may become more difficult compared with pure Ar RF-ICPs^[30].

In order to find the power-up process of Ar-N₂ RF-ICP higher than 50 kW, thermal flows and the electrical characteristics of Ar-N₂ RF-ICPs were investigated based on the numerical results of 2-dimensional MHD (Magneto-Hydro Dynamic) equations for Ar-N₂ RF-ICP combined with the basic circuit theory. Based on these numerical studies, the optimum N₂ content and the impedance matching system are presented for Ar-N₂ RF-ICPs with the power level of 50 kW. For the suggested Ar-N₂ RF-ICP of 50 kW, then, plasma-particle interactions were examined considering the dense loading effect to simulate the high feeding rate of ≥ 16.7 g/min. From the computational results, process conditions of Ar-N₂ RF-ICP can be suggested for mass production of spherical Ni nano-powders. Finally, RF thermal plasma system with maximum power level of 100 kW was set-up and the experimental works were carried out to demonstrate the feasibility of analysis results on RF thermal plasma process for the mass production of nickel nanoparticles. In Fig. 1.4, the objectives and the approach of the present work were briefly displayed.

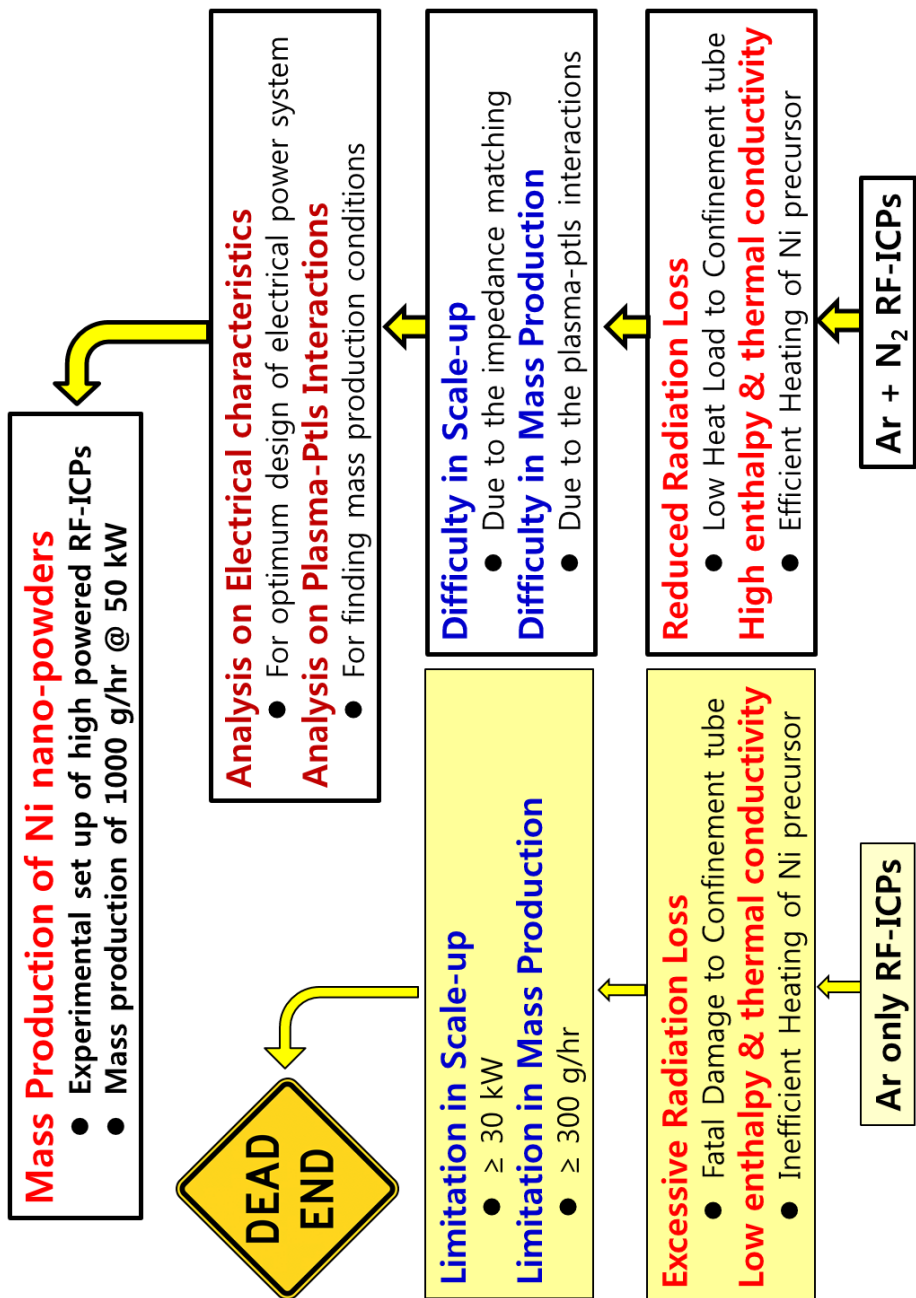


Figure 1. 4 A schematic of objectives and approach of the present work

Chapter 2. Numerical model

2.1. Computational domain and basic assumptions for RF-ICP simulation

Figure 2.1 presents a schematic of the RF-ICP torch adopted in this work for high powered Ar-N₂ RF-ICP simulation. In this figure, carrier gas (Q₁) is injected into RF-ICP torch through a precursor injector with the inner radius of R₁. The sheath gas (Q₃) passes through an annular channel between the intermediate tube and the confinement tube wall while the central gas of flow rate Q₂ is also introduced between R₂ and R₃. All of these plasma gases are assumed as Ar-N₂ mixture with a given content of N₂. An induction coil with the turn number of 4 is located at z = Z_C away from the torch inlet of z = 0. The turning radius of induction coil and the frequency are fixed at R_C = 56.25 mm and f = 2 MHz, respectively, taking into account the high power level of 50 kW and the relatively large diameter of confinement tube wall. Details on other torch dimensions and operating conditions are summarized in Table 2.1 for the present numerical work. The computational domains are divided by rectangular grids and the numbers of mesh cells generated by these grids are 3250 inside the RF torch. All governing equations are discretized by the finite volume method (FVM) and calculated using the SIMPLE algorithm^[31].

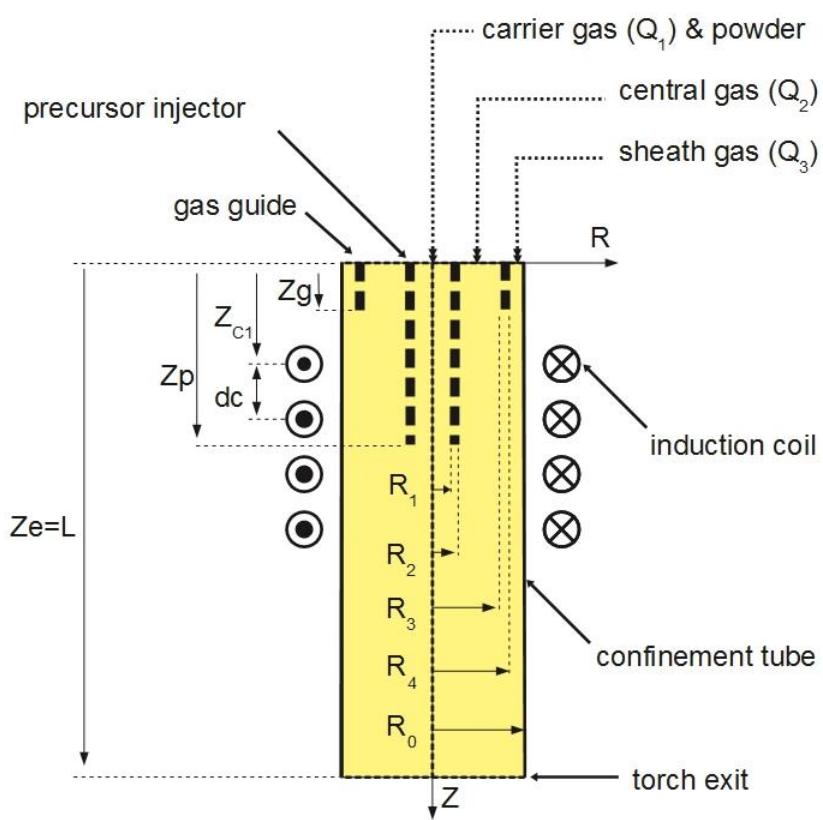


Figure 2. 1 Schematic of RF induction torch.

Table 2. 1 Principal design and operation parameters for ICP torch

Symbol	Description	Value	Unit
P_{RF}	RF input power	50	[kW]
Q_1	Carrier gas flow rate	5	[lpm]
Q_2	Central gas flow rate	50	[lpm]
Q_3	Sheath gas flow rate	150	[lpm]
R_1	Inner radius of precursor injector	3.5	[mm]
R_2	Outer radius of precursor injector	6	[mm]
R_3	Inner radius of guide tube	38	[mm]
R_4	Outer radius of guide tube	42	[mm]
R_0	Inner radius of confinement tube	45.5	[mm]
R_c	Turn radius of induction coil	56.25	[mm]
f	Oscillating frequency	2	[MHz]
N	Number of coil turns	4	
d_c	Gap distance of induction coil	12.5	[mm]
Z_{CI}	Axial position of the first turn of RF coil	140	[mm]
Z_p	Axial position of powder injector tip	160	[mm]
L	Torch length	500	[mm]

In this numerical work, the two-dimensional (2-D) simulations on the induction thermal plasma inside the torch region are carried out with the usual assumptions frequently used in the previous thermal plasma modeling^{[19], [32]}:

- (1) The thermal plasma flow is 2-D axisymmetric.
- (2) The produced thermal plasma is quasi-neutral and steady.
- (3) The optically-thin thermal plasma is in a local thermodynamic equilibrium (LTE) state.
- (4) The induction plasma inside the torch is laminar flow rather than turbulent flow^{[33], [34]}.
- (5) The terms of viscous dissipation and pressure work are not considered in the energy equation.
- (6) The flow is incompressible and the mass density depends only on the thermal plasma temperature.

Based on these assumptions, the interactions coupled among coil current, induced plasma eddy current, and plasma flow are analyzed in the framework of MHD equations describing the conservation of mass, momentum, and energy, respectively. The cylindrical coordinates system (r , z) is adopted in the 2-D numerical modeling because of its geometrical symmetry about the axis.

2.2. Properties of thermal plasmas

The plasma composition depends heavily on its temperature, which is a result of the energy balance between the electrical energy dissipated in the plasma and the heat losses of the plasma. The thermodynamic properties (enthalpy, entropy, specific heat, etc.) rely strongly upon the composition of the plasma. The plasma composition can be calculated through the principle of minimization of the Gibbs free energy for a given pressure and temperature,

which in turn depends on the chemical potentials of the different chemical species present in the plasma. At high temperatures ($T > 6000$ K), these chemical potentials can be calculated only from statistical thermodynamic considerations through quantities called partition functions, which are related to the internal energy levels of the different chemical species of the plasma.

Transport coefficients, such as viscosity, thermal conductivity, electrical conductivity and diffusion coefficients, are generally calculated using the Chapman-Enskog method^{[35], [36]}, which is based on an approximate solution of the Boltzmann equation^[37]. Expressions for the transport coefficients are derived as functions of the collision integrals, which are averages over a Maxwellian distribution of the binary collision cross sections. Collision integrals are necessary for each pair of species existent in the plasma. They are typically derived from the intermolecular potentials.

The temperature-dependent thermodynamic and transport properties of the plasma are obtained from the literatures^{[38], [39]}, which are calculated with an assumption of the local thermodynamic equilibrium (LTE). The physical properties of the gaseous mixture were calculated by applying the simplified mixing rules to the data of pure Ar and N₂ gases^[38].

2.3. Governing equations for RF-ICP

As a thermal fluid flow, RF-ICP can be described by the well-known conservation equations of mass, momentum and energy.

-Continuity equation

$$\nabla \cdot (\rho \vec{u}) = S_p^C \quad (1)$$

where z and r are the axial and radial coordinates, ρ is the mass density, and u and v are the axial and radial components of velocity, respectively.

-Momentum conservation equations

The azimuthal component of velocity is also calculated to consider swirl motion of the plasma even though the two-dimensional axisymmetric system is employed.

$$\rho \vec{u} \cdot \nabla \vec{u} = -\nabla p + \nabla \cdot \mu \nabla \vec{u} + \mathbf{J} \times \mathbf{B} + S_p^M \quad (2)$$

-Energy conservation equation

$$\rho \vec{u} \cdot \nabla h = \nabla \cdot \frac{k_{th}}{c_p} \nabla h + \sigma E^2 - Q_r + S_p^E \quad (3)$$

where h , k_{th} , c_p and Q_r are the plasma enthalpy, the thermal conductivity, the specific heat at the constant pressure, and the radiation loss energy, respectively.

$$\rho \vec{u} \cdot \nabla y = \nabla \cdot D \nabla y + S_p^C \quad (4)$$

In the RF-ICP torch, the electromagnetic fields can be derived from the magnetic vector potential \mathbf{A} , which is determined from the following equations [40], [41].

$$A_\theta = A_R + iA_I \quad (5)$$

$$\frac{\partial^2 A_R}{\partial z^2} + \frac{1}{r} \left(r \frac{\partial A_R}{\partial r} \right) - \frac{A_R}{r^2} + \mu_0 \sigma \omega A_I = 0 \quad (6)$$

$$\frac{\partial^2 A_I}{\partial z^2} + \frac{1}{r} \left(r \frac{\partial A_I}{\partial r} \right) - \frac{A_I}{r^2} - \mu_0 \sigma \omega A_R = 0 \quad (7)$$

In the above equations, the subscripts R and I mean the real and imaginary parts of the magnetic vector potential A , respectively, where $i = \sqrt{-1}$. According to Ampere's law and Faraday's law, the magnetic field components B_z , B_r and electric field E are then calculated by

$$E_\theta = -i\omega A_\theta \quad (8)$$

$$\mu_0 H_z = \frac{1}{r} \frac{\partial}{\partial r} (r A_\theta) \quad (9)$$

$$\mu_0 H_r = -\frac{\partial}{\partial z} A_\theta \quad (10)$$

where f is the RF frequency applied to the induction coil. Finally, the Lorentz force and Joule heating are derived by

$$F_r = \frac{1}{2} \mu_0 \sigma \Re [E_\theta H_z^*] \quad (11)$$

$$F_z = -\frac{1}{2} \mu_0 \sigma \Re [E_\theta H_r^*] \quad (12)$$

$$P_J = \frac{1}{2} \sigma [E_\theta E_\theta^*] \quad (13)$$

where the superscript * denotes the complex conjugate.

2.4. Boundary conditions for RF-ICP

Table 2.2 presents a full set of the boundary conditions for the above governing MHD equations, which have been widely adopted in thermal plasma science. For example, the mathematical expression for magnetic vector potential at the confinement tube wall ($r = R_0$) in Table 2.2 is a typical boundary condition representing the equivalent sheet current in the two dimensional (2-D) modeling for RF-ICP [40], [41]. With all the above MHD equations and boundary conditions, the numerical simulation of 2-D RF-ICP can be carried out for the computational domain in Figure 2.1.

Table 2. 2 Boundary conditions for RF-ICP

Inlet ($z = 0$)		
$u = \begin{cases} Q_1/\pi r_1^2 & r < r_1 \\ 0 & r_1 \leq r \leq r_2 \\ Q_2/\pi(r_3^2 - r_2^2) & r_2 < r < r_3 \\ 0 & r_3 \leq r \leq r_4 \\ Q_3/\pi(R_0^2 - r_4^2) & r_4 \leq r \leq R_0 \end{cases} \quad v = 0 \quad T = T_i$		
$\frac{\partial^2 A_R}{\partial z^2} = 0$	$\frac{\partial^2 A_I}{\partial z^2} = 0$	
Symmetric axis ($r = 0$)		
$\frac{\partial u}{\partial r} = 0$	$v = 0$	$\frac{\partial T}{\partial r} = 0$
$A_R = 0$	$A_I = 0$	
Wall ($r = R_0$)		
$u = 0$	$v = 0$	$\lambda \frac{\partial T}{\partial r} = \frac{\lambda_w}{\delta_w} (T_s - T_w)$
$A_R = \frac{\mu_0 I}{2\pi} \sqrt{\frac{R_c}{R_0}} \sum_{i=0}^{coil} G(k_i)$ $+ \frac{\mu_0 \omega}{2\pi} \sum_{i=1}^{C.V.} \sqrt{\frac{r_i}{R_0}} \sigma_i A_{I,i} S_i G(k_i)$	$A_I = -\frac{\mu_0 \omega}{2\pi} \sum_{i=1}^{C.V.} \sqrt{\frac{r_i}{R_0}} \sigma_i A_{R,i} S_i G(k_i)$	
Outlet ($z = L_T$)		
$\frac{\partial(\rho u)}{\partial z} = 0$	$\frac{\partial v}{\partial z} = 0$	$\frac{\partial T}{\partial z} = 0$
$\frac{\partial^2 A_R}{\partial z^2} = 0$	$\frac{\partial^2 A_I}{\partial z^2} = 0$	

2.5. Equivalent circuit and electrical parameter calculation

Figure 2.2 presents a cross sectional view of the induction coil segments and plasma cells carrying coil current I_c and induced plasma current $I_{p,m}$, respectively. In these figures, V_{torch} means the voltage drop in the induction coil and the terms of I , R and L are the current, resistance and inductance, respectively. The subscripts *coil* or *c*, *p* and *eq* indicate the induction coil, plasma and equivalent values, respectively. Including the details on the electrical circuit in Figures 2.3 and 2.4, the related theory can be referred to Seo et al.'s work [42]. In addition, the mathematical formulation for V_{torch} can be expressed as following according to Kim et al.'s suggestion [43]

$$V_{torch} = \sum_l^{coil} 2\pi R_{c,l} \left(\frac{I_c}{\sigma_{coil} S_{coil}} + i\omega A_l \right) \quad (14)$$

where σ_{coil} , S_{coil} and A_l are the electrical conductivity of coil conductor, coil conduction area, and the magnetic vector potential at the l^{th} coil segment, respectively. The magnetic vector potential A_l at the l^{th} coil is completely calculated by the summation of the contribution terms from neighboring coil current as [43]

$$A_l = \sum_n^{coil} \frac{I_c}{2\pi} \Gamma_n - \sum_m^{plasma} j \frac{\mu_0}{2\pi} \sigma_m A_m S_m \sqrt{\frac{r_m}{R_c}} G(k_m) \\ + \sum_s^{surface} \frac{dz_s}{2\pi} \sqrt{\frac{r_m}{R_c}} \left(\frac{\partial A_s}{\partial n} G(k_s) - A_s \frac{\partial G(k_s)}{\partial n} \right) \quad (15)$$

where Γ_n is related to the self and mutual inductances of coil segments and suggested by Kim *et al.* [43] as follows:

$$\Gamma_n = R_{c,l} \mu_0 \sqrt{\frac{R_{c,n}}{R_{c,l}}} G(k_{l,n}), \text{ if } l \neq n ; \quad \Gamma_n = 10^{-9} N^2 R_{c,l} P_f \text{ if } l = n \quad (16)$$

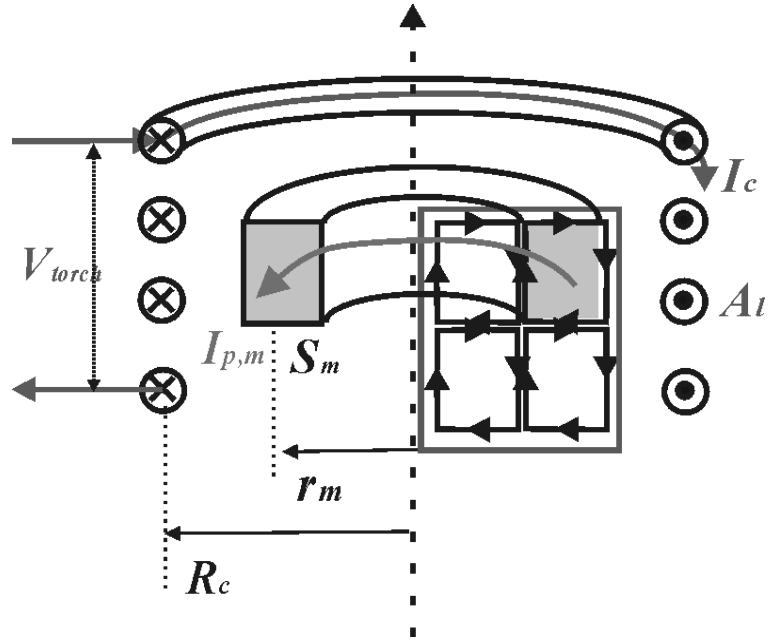


Figure 2. 2 A cross sectional view of the induction coil segments and plasma cells.

Here, P_f is the shape factor in Grover's self-inductance formula [44]. If the voltage drop in the induction coil, V_{torch} is obtained, the equivalent resistance R_{eq} and inductance L_{eq} for RF-ICP are calculated by dividing V_{torch} with the coil current I_c as following [42], [43];

$$R_{eq} = \sum_l^{coil} 2\pi R_{c,l} \left[\frac{1}{\sigma_{coil} S_{coil}} + \frac{\mu_0 \omega^2}{2\pi I_c} \sum_m^{plasma} \sigma_m \operatorname{Re}[A_m] r_m S_m \sqrt{\frac{r_m}{R_{c,l}}} G(k_m) \right. \\ \left. + \sum_s^{surface} \frac{\omega dz_s}{2\pi I_c} \sqrt{\frac{r_s}{R_{c,l}}} \left(\operatorname{Im}[A_s] \frac{\partial G(k_s)}{\partial n} - G(k_s) \frac{\partial \operatorname{Im}[A_s]}{\partial n} \right) \right] \quad (17)$$

$$L_{eq} = \sum_l^{coil} 2\pi R_{c,l} \left[\sum_n^{coil} \frac{\Gamma_n}{\omega} - \frac{\mu_0 \omega}{2\pi} \sum_m^{plasma} \sigma_m \operatorname{Im}[A_m] r_m S_m \sqrt{\frac{r_m}{R_{c,l}}} G(k_m) \right. \\ \left. + \sum_s^{surface} \frac{dz_s}{2\pi} \sqrt{\frac{r_s}{R_{c,l}}} \left(\operatorname{Re}[A_s] \frac{\partial G(k_s)}{\partial n} - G(k_s) \frac{\partial \operatorname{Re}[A_s]}{\partial n} \right) \right] \quad (18)$$

According to the transformer theory, electrical circuit for RF-ICP system and its equivalent circuit can be presented as shown in Figures 2.3 and 2.4, respectively. Since the dissipated RF power P_0 and the total magnetic power P_{mag} , can be represented with the terms of equivalent resistance R_{eq} and inductance L_{eq} as following equations (19) and (20), respectively, the electrical coupling efficiency of RF-ICP, h_c can be obtained by using equation (21) according to its definition.

$$P_0 = \frac{1}{2} I_c^2 (R_{eq} - R_{coil}) \quad (19)$$

$$P_{mag} = \frac{1}{2} I_c^2 \omega L_{eq} \quad (20)$$

$$\eta_c \equiv \frac{P_0}{P_{mag}} = \frac{R_{eq} - R_{coil}}{\omega L_{eq}} \quad (21)$$

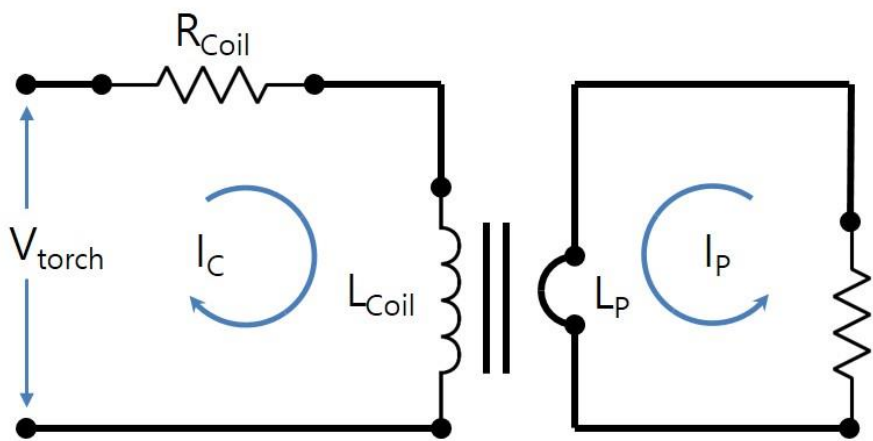


Figure 2. 3 Electrical circuit of RF ICP.

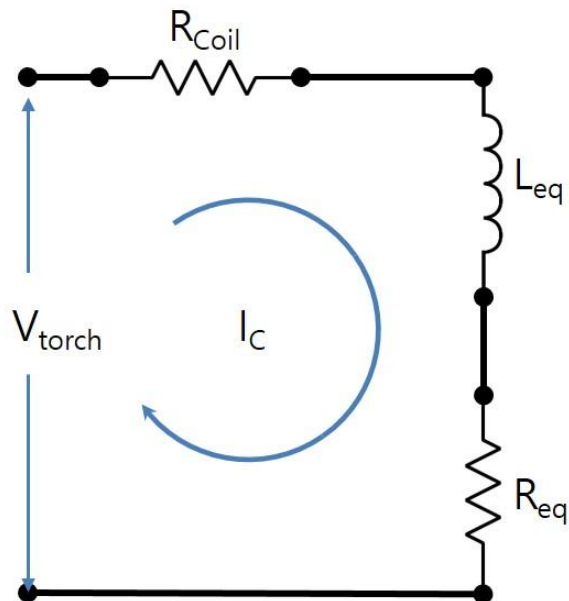


Figure 2. 4 Equivalent circuit of RF ICP.

2.6. Plasma-particle interactions: Particle trajectory and temperature history

Single particle trajectories were calculated by solving a simplified form of the Basset-Boussinesq-Oseen equation as given by the following equations for the axial and radial movement of the particles respectively.

$$\frac{du_p}{dt} = -\frac{3}{4} C_D (u_p - u) U_R \left(\frac{\rho}{\rho_p d_p} \right) + g \quad (22)$$

$$\frac{dv_p}{dt} = -\frac{3}{4} C_D (v_p - v) U_R \left(\frac{\rho}{\rho_p d_p} \right) \quad (23)$$

The above equations were derived assuming that the only forces which influenced the trajectory of the particles were the drag and the gravity forces. Calculations were made of the axial and radial velocity components assuming that the particles to be spherical and to enter the torch at the same velocity as that of the carrier gas. This meant that all the particles had a zero initial radial velocity, and that particles at different initial radial positions in the powder feed tube, would enter the torch at different initial axial velocities for the same carrier gas flow rate.

The drag coefficients used in the solution of equations (22) and (23) were estimated as function of the particles Reynolds number of the following equations.

$$C_D = \begin{cases} \frac{24}{Re} & Re \leq 0.2 \\ \frac{24}{Re} \left(1 + \frac{3}{16} Re\right) & 0.2 < Re \leq 2.0 \\ \frac{24}{Re} \left(1 + 0.11 Re^{0.81}\right) & 2.0 < Re \leq 21.0 \\ \frac{24}{Re} \left(1 + 0.189 Re^{0.62}\right) & 21.0 < Re \leq 200 \end{cases} \quad (24)$$

The Reynolds number was calculated using the particle diameter and the relative velocity between the particle and the gas, U_R , defined as

$$U_R = \sqrt{(u_p - u)^2 + (v_p - v)^2} \quad (25)$$

The instantaneous particle temperature was determined by an energy balance on the particle represented by equations, (26) and (27).

$$Q = \pi D_p^2 h_c (T - T_p) - \pi D_p^2 \sigma_S \varepsilon (T_p^4 - T^4) \quad (26)$$

$$Q = \begin{cases} \rho_p \left(\frac{\pi}{6} D_p^3\right) c_p \frac{dT_p}{dt} & \text{for } T_p < T_m \text{ or } T_m < T_p < T_b \\ \rho_p \left(\frac{\pi}{6} D_p^3\right) H_m \frac{dx}{dt} & \text{for } T_p = T_m \\ -\rho_p \left(-\frac{\pi}{2} D_p^2\right) H_v \frac{dD_p}{dt} & \text{for } T_p = T_b \end{cases} \quad (27)$$

The heat transfer coefficient, h_c was calculated using the following relation^[28]:

$$Nu = \frac{h_c D_p}{k} = 2.0 + 0.515 Re^{0.5} \quad (28)$$

When the temperature of particle reached its melting point ($T_m = 2323$ K), its temperature was assumed to remain constant. The liquid fraction, x , of the particle was then calculated using the equation (26) and the second term of the equation (27). Once the particle was completely molten ($x = 1$), its temperature was allowed to rise again till it reached its boiling point ($T_b = 3005$ K). At this point, the particle temperature remained constant and its diameter decreased due to evaporation as indicated by equation (26) and the third term of the equation (27). Finally, the calculations were stopped as the particle diameter becomes of the order of 10 nm. At this stage the particle was assumed to be completely evaporated.

2.7. Plasma-particle interactions: Particle Source In Cell (PSI-Cell) Model

The simulation for plasma-particle interactions in this work is based on PSI-Cell concept developed by Crowe and co-workers^[45] and adapted to the RF plasma torch system by Proulx et al.^{[28], [29]}. In this model, the momentum, mass, and energy exchange rates per unit volume between the gas phase and the particles are introduced as source/sink terms in the corresponding conservation equations for the gas and particle phases. An iterative technique involving the solution of the gas-phase conservation equations and the solution of the particle trajectories is used until the convergence conditions are met. According to the PSI—Cell model, the passage of a particle through a cell can cause the exchange of momentum, energy and mass between the particle and the fluid in that cell. In order to account for such exchanges, it is necessary to calculate appropriate source-sink terms defined as S_p^c , $S_p^{M_r}$, $S_p^{M_z}$ and S_p^E , respectively.

Firstly, let N_t^0 be the total number of particles injected per unit time, n_D is the particle size distribution, and n_r represents the fraction of N_t^0 injected at each point over the central tube radius. The total number of particles per unit time travelling along the trajectory (l, k) corresponding to a particle diameter D_{pl} injected at the point r_k is:

$$N_{(l,k)}^0 = n_D n_{rk} N_t^0 \quad (29)$$

The particle concentration in a given cell crossed by the trajectory (l, k) is

$$C_i^{(l,k)} = \frac{N_{(l,k)}^0 \tau_i^{(l,k)}}{V_i} \quad (30)$$

Where $\tau_i^{(l,k)}$ is the residence time of the (l, k) particles in the (i) cell of volume V_i . The mass source term for the (i) cell, $S_{p,i}^c$, is given as

$$S_{p,i}^c = \sum_{l,k} C_i^{(l,k)} \frac{\Delta m_p^{(l,k)}}{\tau_i^{(l,k)}} \quad (31)$$

due to all the trajectories with initial diameter D_{pl} and initial injection point r_k . The term, $\Delta m_p^{(l,k)}$ is the amount of mass evaporated by a particle with (l, k) trajectory in cell (i) . The corresponding source term, $S_{p,i}^E$, in the energy equation includes the heat given to the particles $Q_{p,i}^{(l,k)}$, as well as the superheat needed to bring the particle vapors into thermal equilibrium with the plasma gas $Q_{v,i}^{(l,k)}$.

$$S_{p,i}^E = \sum_{l,k} C_i^{(l,k)} [Q_{p,i}^{(l,k)} + Q_{v,i}^{(l,k)}] \quad (32)$$

$$Q_{p,i}^{(l,k)} = \frac{1}{\tau_i^{(l,k)}} \int_0^{\tau_i^{(l,k)}} \pi D_p^2 h_c [T_i - T_{p,i}^{(l,k)}] dt \quad (33)$$

$$Q_{v,i}^{(l,k)} = \frac{1}{\tau_i^{(l,k)}} \int_0^{\tau_i^{(l,k)}} \frac{\pi}{2} D_p^2 \rho_p \left(\frac{dD_p}{dt} \right) c_{pV} [T_i - T_{p,i}^{(l,k)}] dt \quad (34)$$

In equation (34), c_{pV} is the specific heat of the particle material in vapor form. The source-sink terms for the corresponding momentum transfer equations are:

$$S_{p,i}^{Mz} = \sum_{l,k} C_i^{(l,k)} \frac{\Delta(m_p u_p)}{\tau_i^{(l,k)}} \quad (35)$$

$$S_{p,i}^{Mr} = \sum_{l,k} C_i^{(l,k)} \frac{\Delta(m_p v_p)}{\tau_i^{(l,k)}} \quad (36)$$

In this work, the energy source term, S_p^E is only calculated for simplicity. A summary of the physical properties of nickel is given in Table 2.3. Their particle size distribution was assumed to be mono-disperse with a particle diameter of 10 μm , 30 μm and 50 μm . Finally, plasma-particle system can be solved through the following steps as illustrated in Figure 2.5.

Step 1. The plasma-governing equations are solved using an iterative method.

Step 2. The trajectories of the discrete particles are calculated for the plasma temperature and velocity fields. These are used for the computation of the integrated source/sink terms which represent the link between the gas phase and the particle-phase conservation equations.

Step 3. These source/sink terms are used by the plasma-governing equations to update the computed plasma and temperature fields taking into account the plasma-particles interaction effects.

Step 4. Steps 2 and 3 are repeated for as many times as needed until convergence of the plasma and particle fields is achieved to a satisfactory level.

Table 2. 3 Physical Properties of Nickel [29]

Property	Symbol	Value	Unit
Mass density	d_p	8,900	kg/m ³
Melting point	T_m	1,727	K
Latent heat of fusion	H_m	0.31	MJ/kg
Boiling point	T_b	3,005	K
Latent heat of vaporization	H_b	0.62	MJ/kg
Specific heat	c_p	0.54	kJ/(kg K)
emissivity	ϵ	0.3	

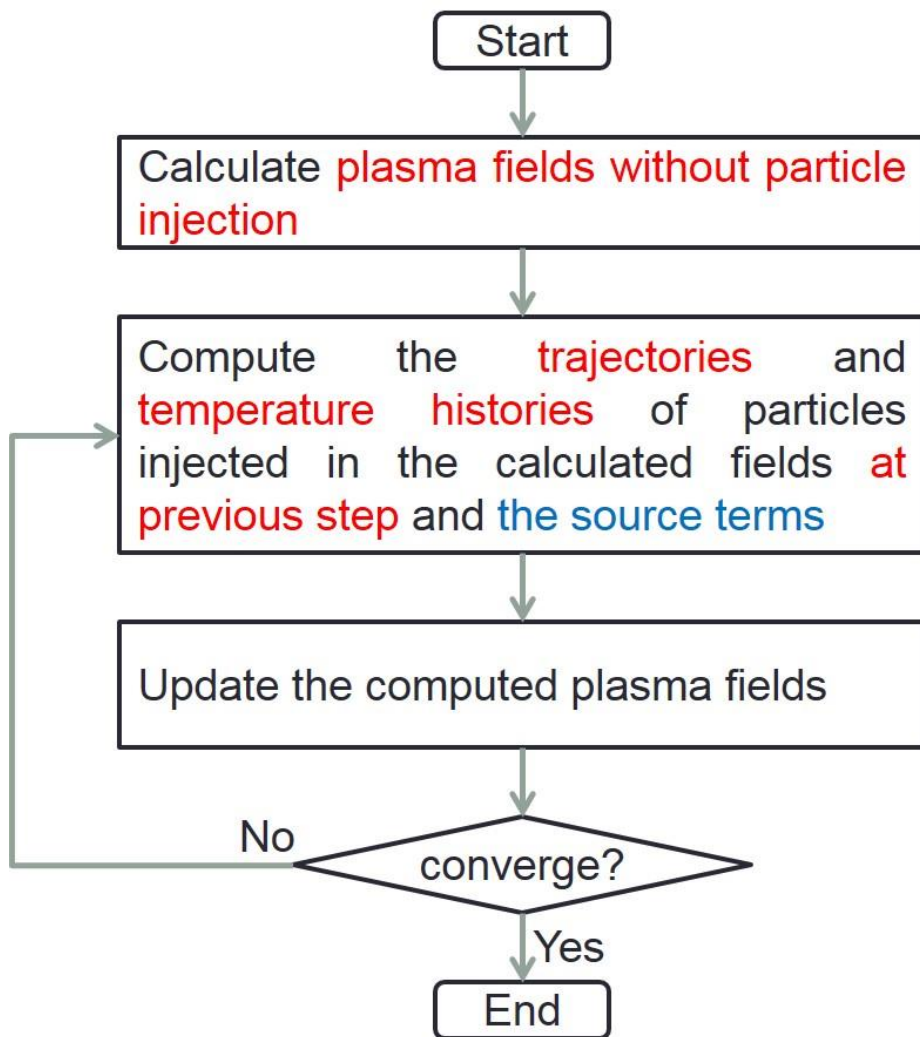
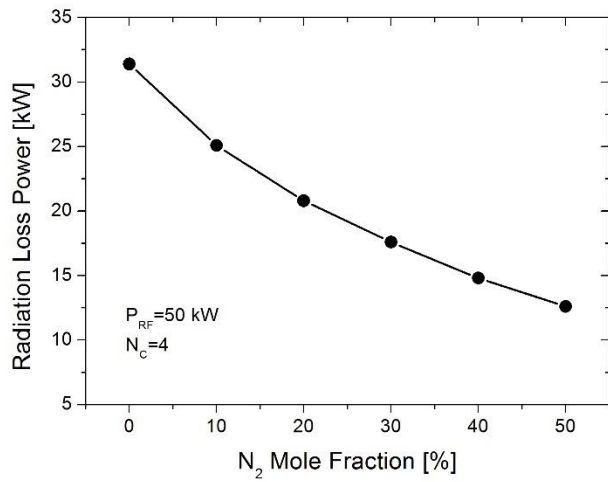


Figure 2. 5 Flow chart of simulation.

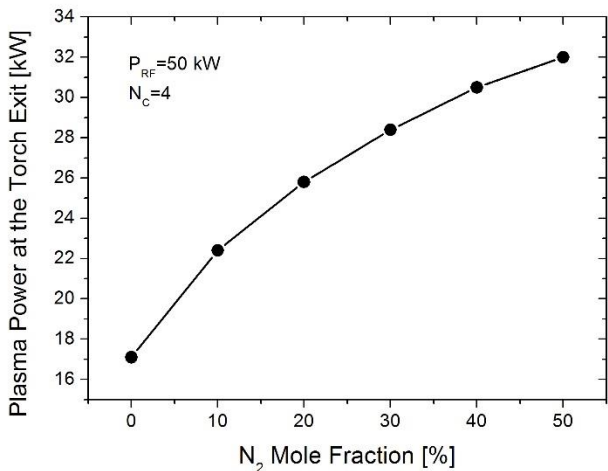
Chapter 3. Numerical analysis of electrical and thermal flow characteristics of Ar-N₂ inductively coupled thermal plasmas

3.1. Effect of N₂ addition on thermal flow characteristics of RF-ICP

As mentioned previously, Ar gas is favorable for easy ignition and stable operation of RF-ICP at a low power level due to its relatively high electrical conductivity compared with other diatomic gases such as N₂. However, at a high power operation, the increased temperatures of Ar plasma induce a rapid increase of radiation power loss, which can cause crucial damage to the confinement tube of the torch. Consequently, for Ar only RF-ICP, it is difficult to scale-up the plasma power to higher than 50 kW, as shown in Figs 3.1(a) and 3.1(b), which present the radiation power losses and the exit enthalpies for N₂ mole fractions calculated at plasma power level of 50 kW, respectively. In Fig. 3.1(a), it can be seen that the radiation power loss can reach about 70% of the RF input power for Ar only RF-ICP. However, Fig. 3.1(a) also shows that, with the addition of N₂, the percentage of radiation power loss can be reduced to about 13% at the N₂ content of 50 mol %. As presented in Fig. 3.1(b), this reduction of radiation loss induces an increase in the exit enthalpy, which means that the thermal efficiency of the RF-ICP torch can be improved by increasing the mole ratio of N₂ gas with the increase of RF input power.



(a)



(b)

Figure 3. 1 (a) Radiation power losses and (b) exit enthalpies calculated for N_2 mole fractions from 0% to 50% at RF power level of 50 kW.

Accordingly, the addition of a secondary gas, such as N₂ is essential for safe operation of the RF-ICP torch at a power level of 50 kW and higher. These effects of N₂ addition can be confirmed again from the comparison between the thermal flow fields of Ar only and Ar-N₂ RF-ICPs at the same operation conditions.

Figures 3.2(a) and 3.2(b) show the temperature contours of Ar only and Ar-N₂ RF-ICPs calculated for the N₂ contents of 0 mol % and 20 mol %, respectively, at the same power level of 50 kW. From these figures, it is observed that the highest temperature region of \sim 10,000 K is significantly diminished for Ar-N₂ RF-ICP with the N₂ content of 20 mol %, which is attributed to the reduction of radiation power loss for N₂ addition.

Figures 3.3(a) and 3.3(b) compare the radial distributions of temperatures and velocities calculated at the torch exit plane for the N₂ contents of 0 mol % and 20 mol %, respectively. As shown in these figures, the high temperature region of $>$ 4,000 K expands radially at the torch exit plane for an N₂ content of 20 mol %, although the temperatures and velocities are reduced slightly at the central region. As a result, the exit enthalpy can be increased with the addition of N₂ compared with Ar only RF-ICP, as discussed previously in Fig. 3.1(b).

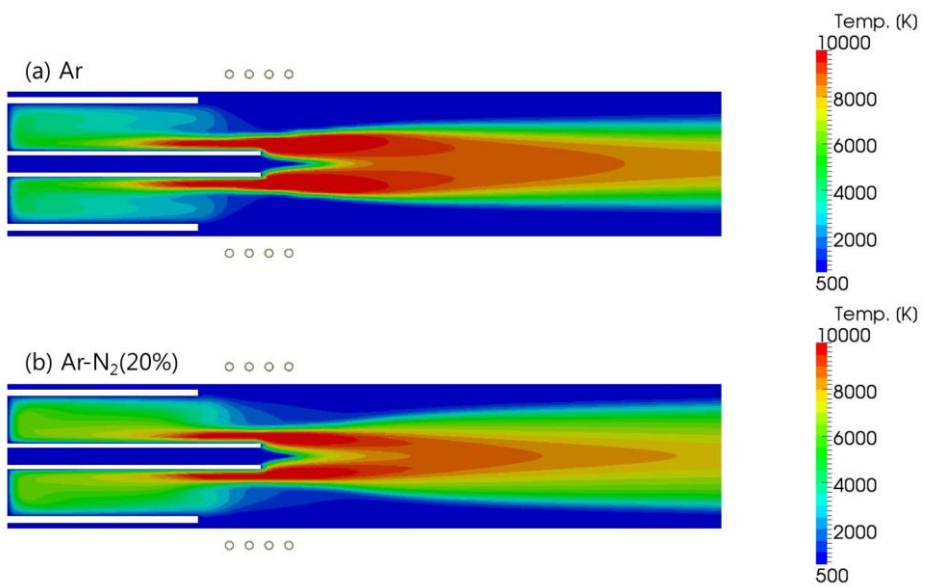
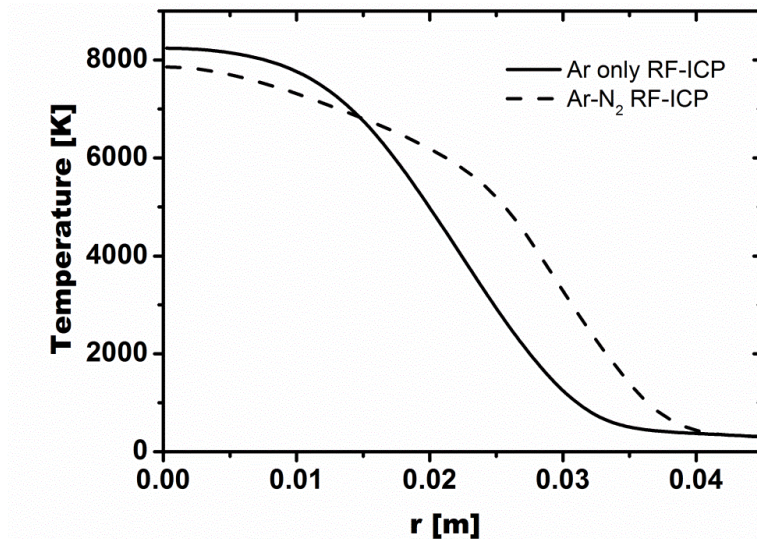
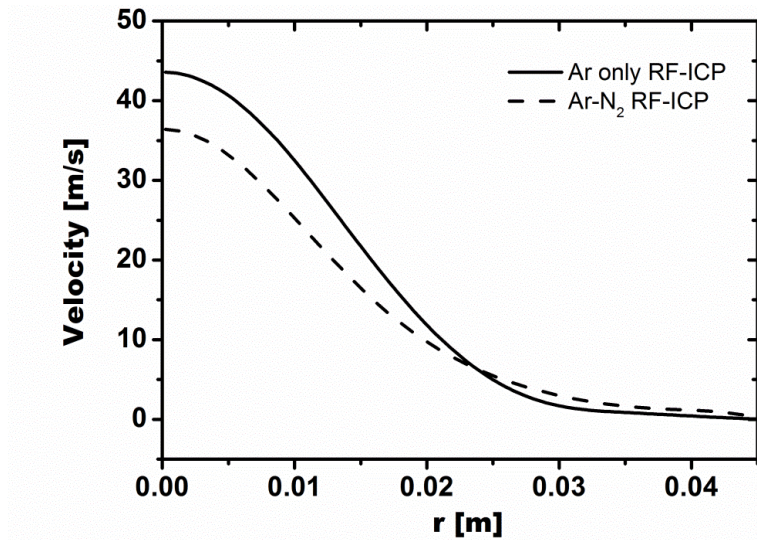


Figure 3. 2 Comparison of temperature contours between (a) Ar only and (b) Ar-N₂ RF-ICPs calculated at plasma power level of 50 kW. For Ar-N₂ RF-ICP, N₂ content is 20 mol %.



(a)

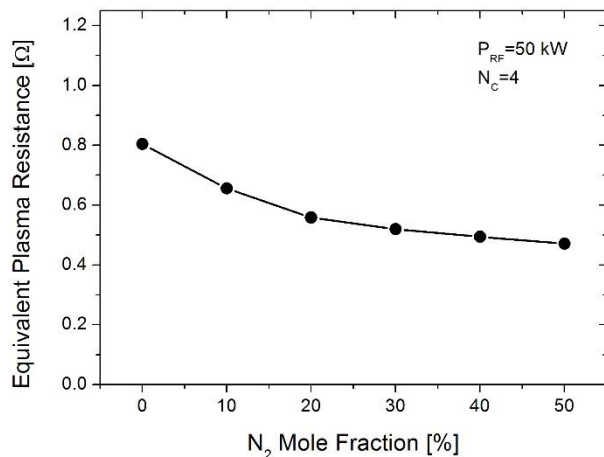


(b)

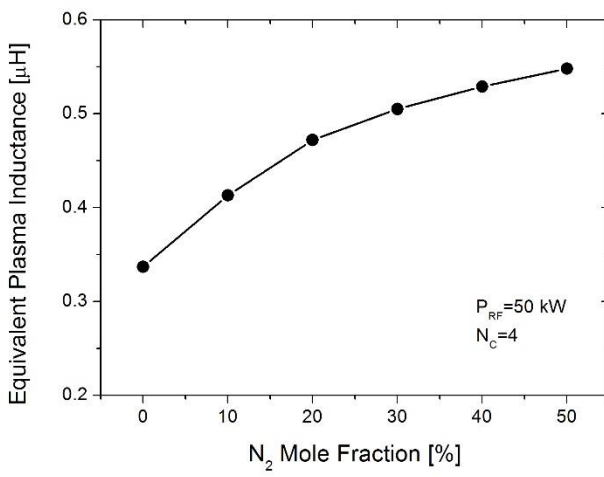
Figure 3. Comparison of Radial distributions of (a) temperatures and (b) velocities at torch exit plane calculated for Ar only and Ar-N₂ RF-ICPs. For Ar-N₂ RF-ICP, N₂ content is 20 mol %.

3.2. Effect of N₂ addition on electrical characteristics of RF-ICP

Corresponding to the changes in thermal flow characteristics, the electrical parameters of RF-ICP are also varied with the addition of N₂ as shown in Figs. 3.4(a) and (b), which present the equivalent values of plasma resistance and inductance for mole ratios of N₂ to Ar calculated at a power level of 50 kW, respectively. From these figures, the equivalent electrical resistance, R_{eq} is observed to decrease with the increase of N₂ mole fraction while equivalent electrical inductance, L_{eq} increases. First, the decrease of equivalent resistance, R_{eq} demonstrates that a greater coil current is required at the same power level in order to sustain Ar-N₂ RF-ICPs compared with Ar only RF-ICP, according to equation (18). Fig. 3.5 shows the calculation results for coil currents increasing with the elevation of N₂ mole fraction. In addition, the behaviors of equivalent inductance, L_{eq} shown in Fig. 3.4(b) indicate that the electrical coupling efficiency can be deteriorated by N₂ addition as shown in Fig. 3.6, which present the electrical coupling efficiencies calculated from equation (20) for N₂ contents from 0 mol % to 50 mol %. In terms of the vacuum tube oscillators employed as a RF power supply in our work, the above effects of N₂ addition to the coil current imply that a tank circuit should be designed to induce high RF currents from the vacuum tube in order to produce a high powered Ar-N₂ RF-ICP.



(a)



(b)

Figure 3. 4 (a) Equivalent plasma resistance and (b) equivalent plasma inductance calculated for N_2 mole fractions from 0% to 50% at RF power level of 50 kW.

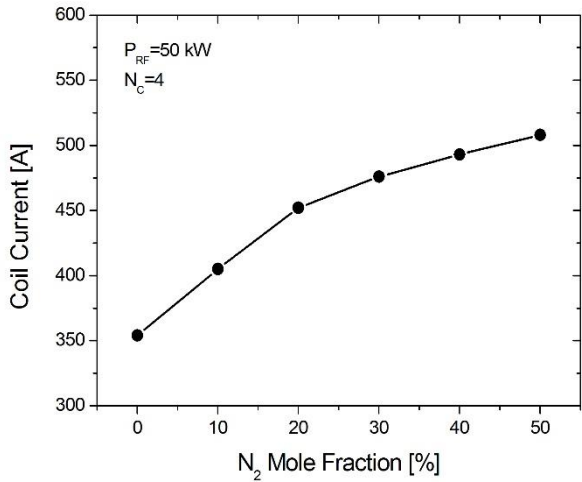


Figure 3. 5 Coil currents calculated for N₂ mole fractions from 0% to 50% at power level of 50 kW.

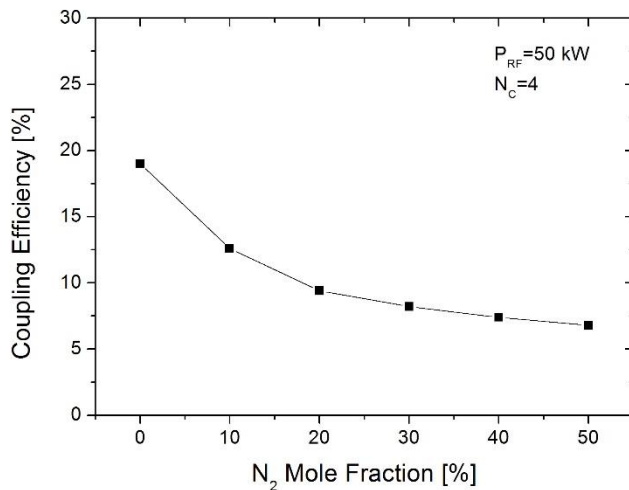


Figure 3. 6 Coupling efficiencies calculated for N₂ contents from 0 mol % to 50 mol % at power level of 50 kW

Normally, the tank circuit for a vacuum tube oscillator consists of capacitors in parallel connection with the equivalent resistance and inductance of the RF-ICP torch as shown in Fig. 3.7. From the basic resonance circuit theory [46], the absolute value of total impedance shown in Fig. 3.7 can be expressed in terms of equivalent resistance R_{eq} , equivalent inductance L_{eq} , and capacitance of tank circuit C_t as follows

$$|Z_t| \approx \frac{1}{2\pi f C_t} \sqrt{1 + \left(\frac{2\pi f L_{eq}}{R_{eq}} \right)^2} \quad (36)$$

where f refers to the resonance frequency of the tank circuit. As expected, in equation (36), the total impedance of the tank circuit increases with the N₂ addition according to the calculation results of Fig. 3.4 for R_{eq} and L_{eq} . Consequently, the demand for high RF current can be fulfilled by determining the capacitance in order to reduce the increased impedance of the tank circuit with the N₂ addition. In other words, the design of the tank circuit for high powered Ar-N₂ plasma could be a key technology in the scale-up of RF-ICP systems with a vacuum tube oscillator. Our calculation results can provide practical information on the electrical characteristics of high powered Ar-N₂ RF-ICPs for the design of the tank circuit for high powered Ar-N₂ plasma.

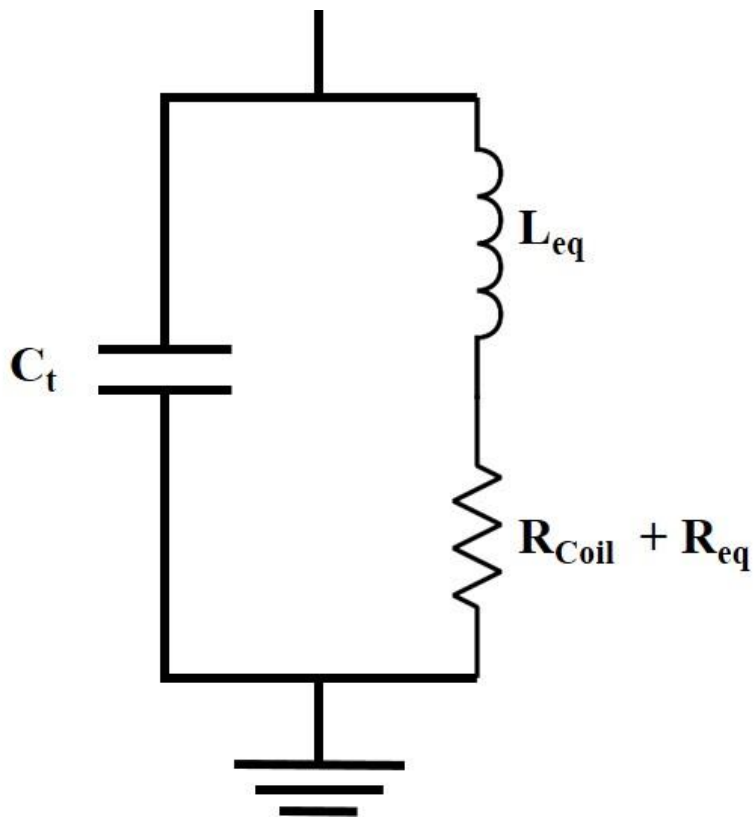


Figure 3. 7 Resonance tank circuit consisting of a capacitor in parallel connection with an equivalent resistance and an equivalent inductance of an RF-ICP

Chapter 4. Simulations on RF induction plasma characteristics and the particle behavior injected into the plasma

4.1. Effect of carrier gas flow rate

In this section, we investigated the effects of carrier gas flow rate on the flow fields of RF thermal plasma with the power level of 50 kW and the behavior of a single particle injected into the torch. Fig. 4.1 (a) shows typical temperature fields of Ar RF-ICP obtained from numerical computation without carrier gas ($Q_1 = 0$ slpm). In this figure, one can see that temperature peaks is off-axis in the coil region due to the electrical skin effect, which is well-known in RF thermal plasma modelling. Fig. 4.1 (b) and (c) present the temperature fields of Ar RF-ICP corresponding to carrier gas flow rates of $Q_1 = 3$ slpm and $Q_1 = 4$ slpm, respectively. A comparison between these three figures (Fig. 4.1 (a), (b) and (c)) reveals that the introduction of cold carrier cools down the central region of Ar RF-ICP along the centerline. In addition, the cooled down zone is axially expanded with the increase of the carrier gas flow rate. This effect of carrier gas flow rate is also checked in Fig. 4.2 comparing temperature fields of $Q_1 = 3$ slpm and $Q_1 = 4$ slpm for induction coil turn number of 4. For effective heating of the injected precursor, thus, the carrier gas flow rate should be minimized as much as possible regardless of RF-ICP torch types.

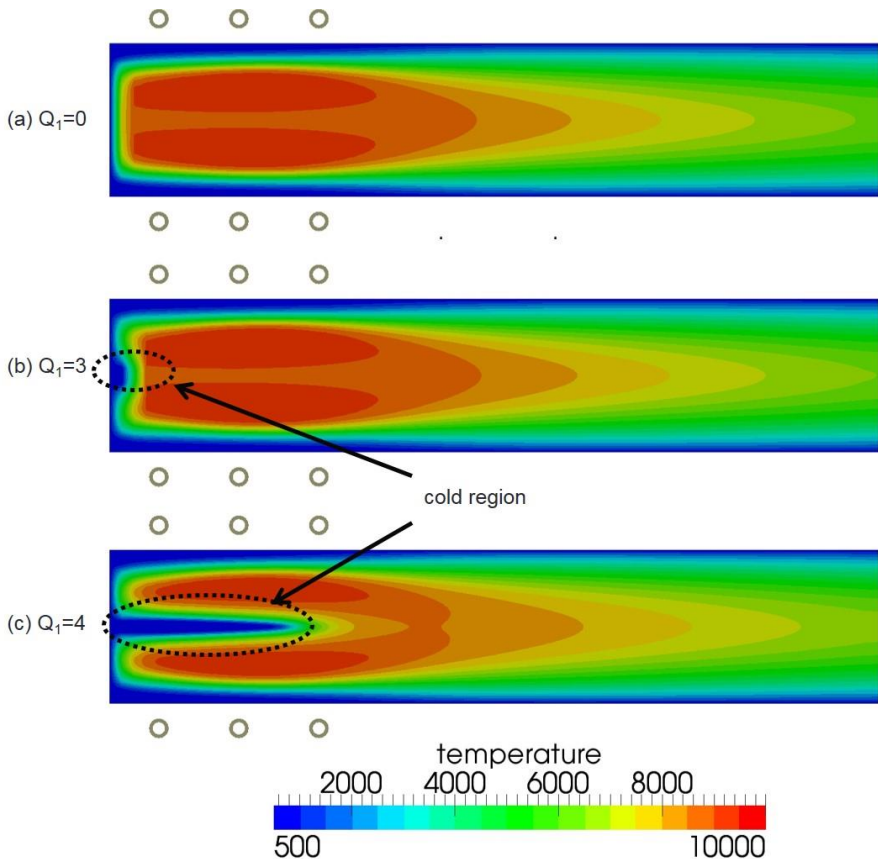


Figure 4. 1 Temperature fields of Ar RF-ICPS at carrier gas flow rates of
(a) $Q_1 = 0$ slpm, **(b)** $Q_1 = 3$ slpm and **(c)** $Q_1 = 4$ slpm

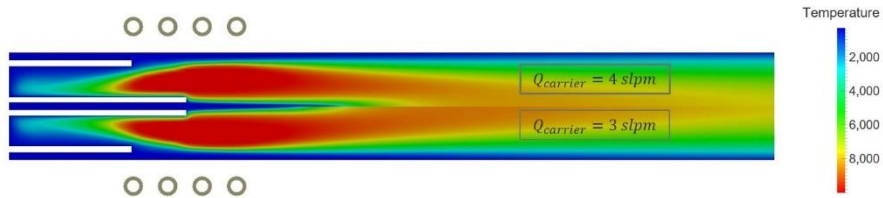


Figure 4.2 Comparison between temperature fields of Ar RF-ICPs at carrier gas flow rates of $Q_1 = 4 \text{ slpm}$ (upper part) and (c) $Q_1 = 3 \text{ slpm}$ (lower part) for induction coil turn number of 4

Figure 4.3 describes the behaviors of Ni particle injected into Ar RF-ICP at carrier gas flow rates of 4 slpm and 3 slpm, respectively. In order to investigate the effect of Ni size on the trajectories and temperature history, computations were carried out for single Ni particle with four different diameters of 1, 5, 10 and 20 μm . As observed in the trajectories of Fig. 4.3, firstly, the injected Ni particle moves along the centerline of the torch and experiences heating process by ambient hot plasma flame. During the heating process, the surface temperatures of the Ni particle reach melting point (1728 K) immediately regardless of particle diameter, then, Ni particle starts melting and transforming into the Ni liquid droplets. In addition, the successive heating process brings Ni droplets to boiling point (3186 K) and evaporates them with the decrease of particle radius for both cases of carrier gas flow rates. As the carrier gas flow rate increases from 3 slpm to 4 slpm, however, the central region of plasma is cooled down with the increase of axial velocity as discussed in Fig. 4.1.

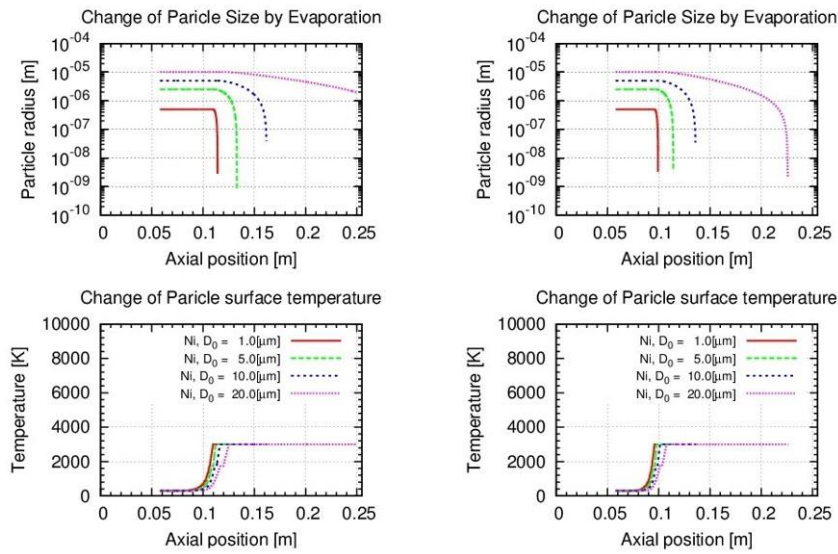


Figure 4.3 Trajectories and temperature histories of precursor Ni particle with diameters of 1, 5, 10 and 20 μm at carrier gas flow rates of $Q_1 = 4 \text{ slpm}$ (left part) and $Q_1 = 3 \text{ slpm}$ (right part).

In this case, the residence time of particle in high temperature region is decreased, then, even a nickel particle with a diameter of 20 μm is difficult to completely vaporize at the power level of 13.5 kW as shown in figure 4.3 (left part).

4.2. Effect of N₂ addition

Figure 4.4 shows changes in size and temperature histories of precursor Ni particles starting at different radial points (from 0.75 mm to 3.75 mm) for Ar only (left part) and Ar-N₂ (right part) RF-ICPs with the power level of 50 kW. Firstly, one can see in this figure that Ni particles injected into pure Ar RF-ICP are difficult to be fully evaporated. On the other hand, Ni particles in Ar-N₂ RF-ICP experience immediate heating process by hot plasma, which has higher enthalpy and thermal conductivity compared to pure Ar plasma.

Figure 4.5 shows changes in size and temperature histories of precursor Ni particles starting at different radial points (from 0.0 mm to 3.0 mm) for Ar-N₂ RF-ICPs with N₂ content of 10 mol % (left part) and 20 mol % (right part) with the power level of 50 kW. It is observed that the N₂ addition has a favorable effect on the heat treatment of particles injected in the torch due to the improvement of heat transfer coefficient. In addition, Fig. 4.4 and 4.5 also show that melting and evaporation routes of the injected Ni particle depends on radial starting position of the injected Ni particle.

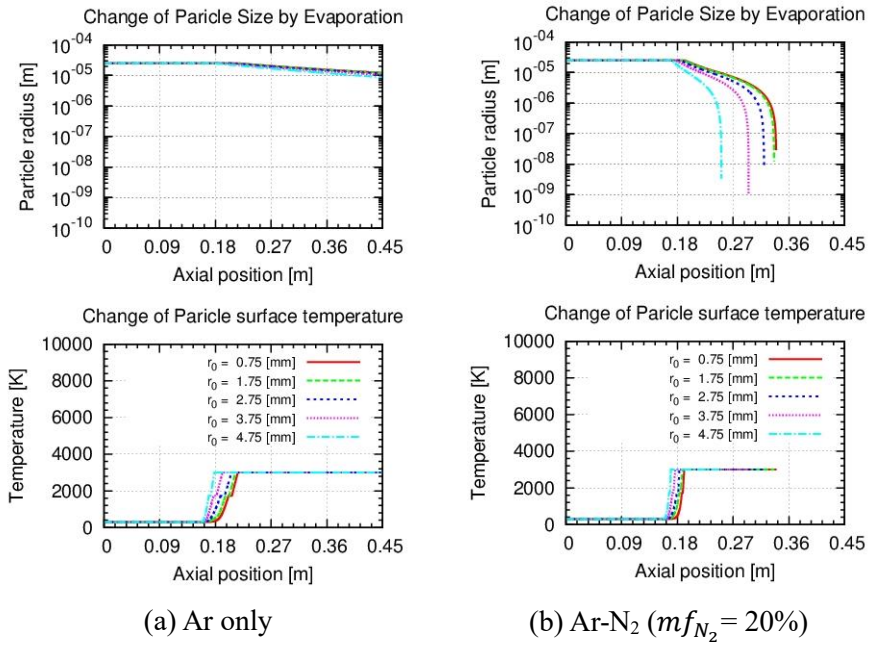


Figure 4. 4 Changes in size and temperature histories of precursor Ni particles starting at different radial points for Ar only (left part) and Ar-N₂ (right part) RF-ICPs with the power level of 50 kW.

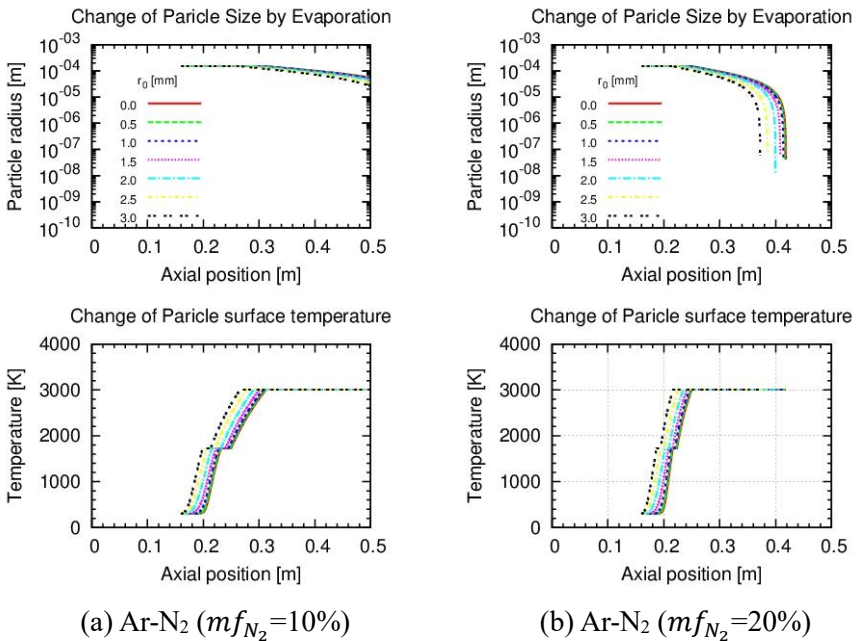


Figure 4.5 Changes in size and temperature histories of precursor Ni particles starting at different radial points for Ar-N₂ RF-ICPs with N₂ content of 10 mol % (left part) and 20 mol % (right part) with the power level of 50 kW

4.3. Effect of Ni feed rate

In this section, the effects of nickel feed rate on the plasma-particle interactions are investigated. For this purpose, dense loading effect is considered based on PSI-Cell model introduced in section 2.6.

Figure 4.6 shows the temperature fields simulated at the RF input power of 50 kW for Ni feed rates of 0.0 g/min and 1.0 g/min. As compared in these figures, the loading of Ni precursor even at the feed rate of 1.0 g/min causes the changes in temperature fields as a result of plasma-particle interactions. In this figure, one can see that hot region of the plasma is diminished for Ni feed rates of 1.0 g/min compared with ones without Ni feeding. In addition, the temperatures along the centerline are decreased for the case of Ni loading at 1.0g/min. In spite of temperature decrease, it is also observed that the temperatures along the centerline are kept higher than 4,000 K, which may be enough for full evaporation of the injected Ni particles. However, the changes in temperature fields are enhanced for high feeding rate of 10.0 g/min as presented in Fig. 4.7 comparing between the temperature fields for Ni feed rates of 0.0 g/min and 10.0 g/min. In this figure, the temperatures are significantly decreased down to 2,000 K along the centerline, and consequently, the complete vaporization of the injected particles seems to be relatively difficult along the centerline trajectories.

This preferential evaporation depending on trajectories and feeding rates can be confirmed in Fig. 4.8, showing the changes in particle sizes calculated along six different trajectories in the Ar(80%) - N₂(20%) RF-ICP at the power level of 50 kW for Ni feeding rates of 10.0 g/min, 20.0 g/min and 40.0 g/min. As can be seen in this figure, all of the injected nickel particles are fully vaporized inside the torch regardless of the trajectories for feeding rates of < 20.0 g/min. For Ni feed rate of 40.0 g/min, however, nickel particles travelling

along the centerline can experience incomplete evaporation. The trajectories showing the incomplete evaporation are increased for high Ni feed rate, then, only about 66.7% of the injected nickel particles is expected to vaporize for Ni feed rate of 40.0 g/min.

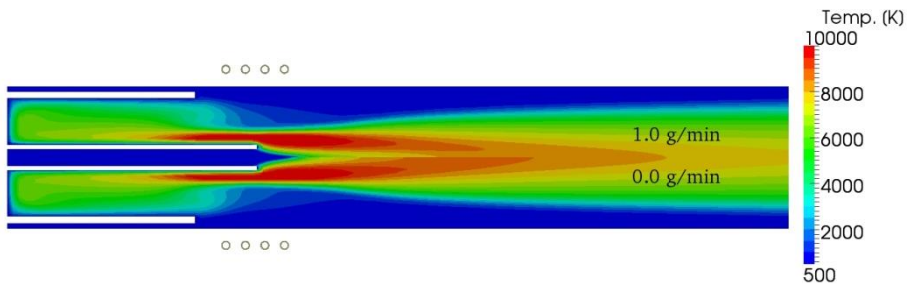


Figure 4.6 Temperature fields simulated at the RF input power of 50 kW for Ni feed rates of 0.0 g/min (bottom) and 1.0 g/min (top).

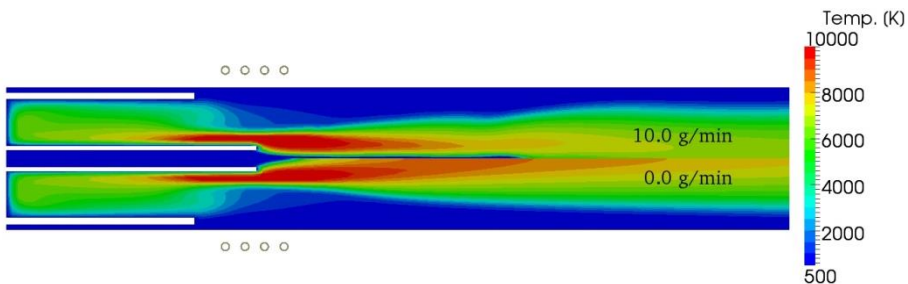


Figure 4.7 Temperature fields simulated at the RF input power of 50 kW for Ni feed rates of 0.0 g/min (bottom) and 10.0 g/min (top).

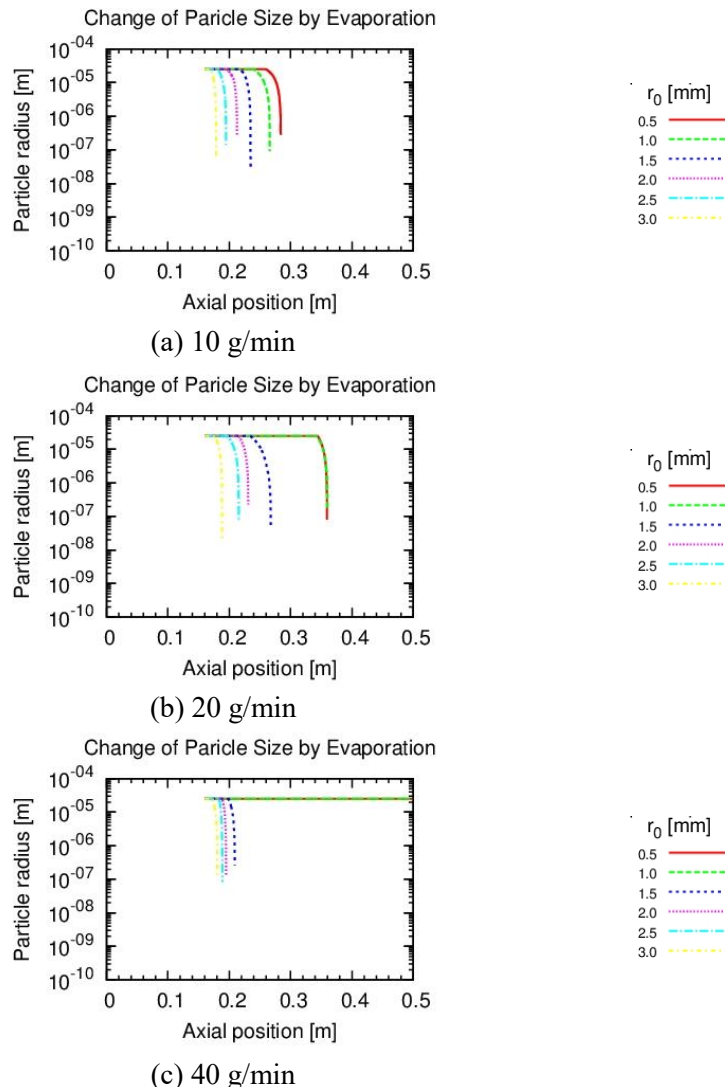


Figure 4.8 Changes in Ni sizes calculated along six different trajectories in the Ar(80%) - N₂(20%) RF-ICP at the power level of 50 kW for Ni feeding rates of (a) 10.0 g/min, (b) 20.0 g/min and (c) 40.0 g/min.

The above numerical results indicate that the incomplete trajectories are not only inevitable but also increased along the centerline with the increase of feed rate due to the quenching effects of carrier gas and solid precursor axially injected along the centerline. As a result, the evaporation rate is decreased with the increase of Ni feed rate as predicted in Fig. 4.9, presenting the evaporation ratio of the axially injected particles according to the Ni feed rate at the same power level of 50 kW.

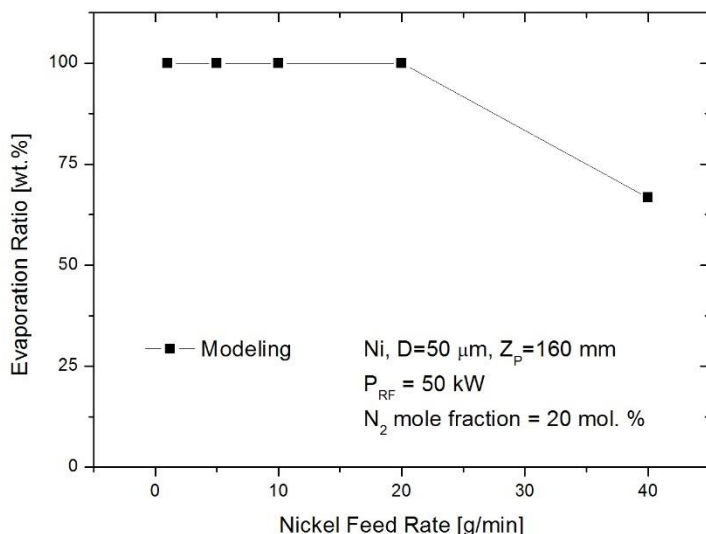


Figure 4. 9 The evaporation ratio of the axially injected particles according to the Ni feed rate at the same power level of 50 kW

4.4. Effect of RF Power

Naturally, the increase of RF input power may be a solution to improve the evaporation rate in Fig. 4.9 because the diminished hot region can be recovered by increasing the electrical energy dissipated in skin depth region. However, the effective heat transfer from the skin depth region to central region along the centerline relies on the heat balance in RF-ICP as well as the electromagnetic energy transfer mechanism of RF-ICP. These effects of RF input power on thermal flow fields of RF ICP are displayed in Figs. 4.10 and 4.11, showing the distributions of temperatures and axial velocities along the centerline and at torch exit plane, respectively, according to the various RF input powers. Firstly, it is found that the increase of RF input power mainly leads to the temperature rising in the off-axis region rather than central region at the torch exit as shown in Fig. 4.10 (a) and 4.11 (a). Accordingly, these effects on the temperature fields can help the full evaporation of Ni particles in trajectories passing the off-axis region. However, Fig. 4.10 (b) and 4.11 (b) show that the increase of RF power input also contributes to the increase of axial velocities in not only centerline region but also off-axis region. Since the increased velocities lead to the decrease of residence time of Ni particles, these effects on the velocity fields can decrease the evaporation ratio of Ni particles in RF thermal plasma process. As a result, these conflicting effects of RF power input can produce an optimum feed rate to maximize the evaporation ratio at a given RF power as presented in Fig. 4.12, showing maximum evaporation ratio of 80% at 50 kW for Ni feed rate of 20 g/min.

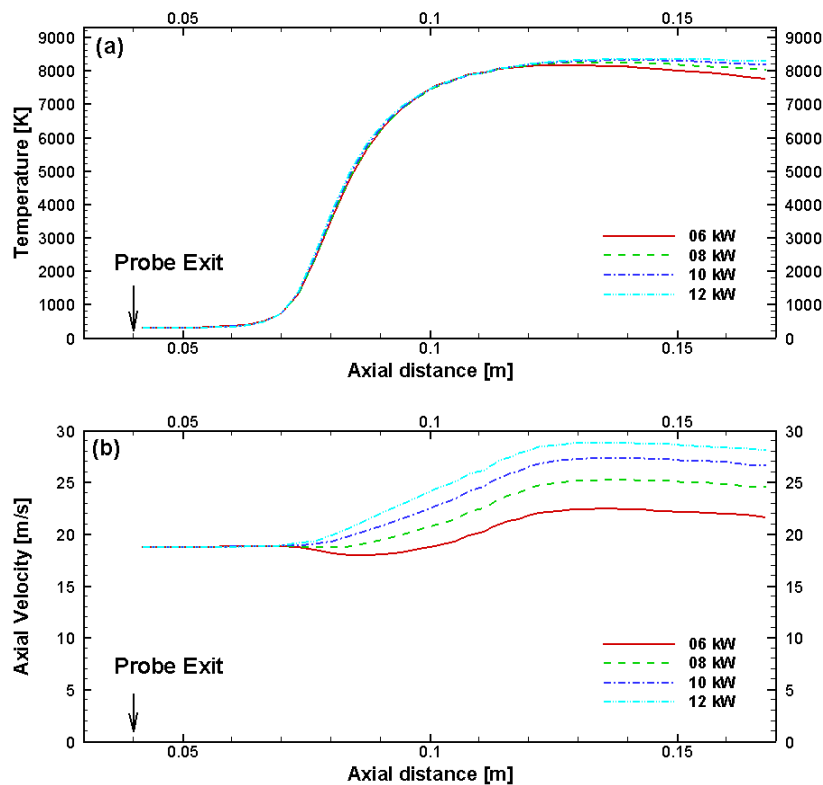


Figure 4. 10 Distributions of temperatures (a) and axial velocities (b) along the centerline according to the various RF input powers without injection of Ni precursor.

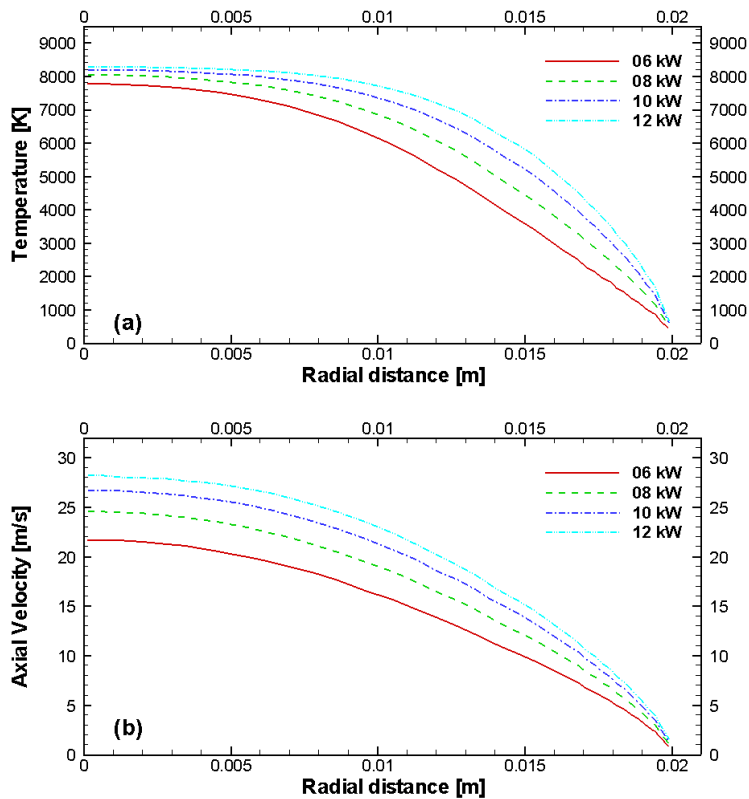


Figure 4.11 Distributions of temperatures (a) and axial velocities (b) at the torch exit plane according to the various RF input powers without injection of Ni precursor.

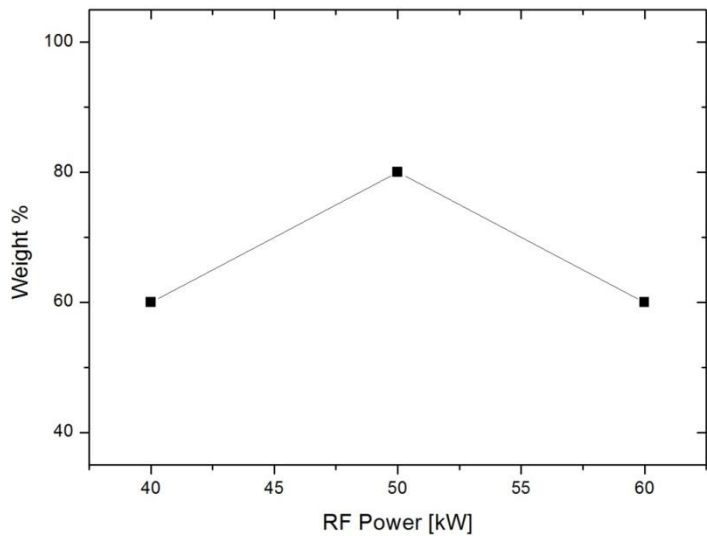


Figure 4. 12 Evaporation ratio of Ni powder injected at the feed rate of 20 g/min for various RF input powers.

Chapter 5. Experiments on mass production of Ni nanoparticles by RF thermal plasma process

5.1. Experimental setup and material characterization

The RF induction thermal plasma system for the synthesis of Ni nanoparticles used in this work was setup as shown in Fig. 5.1. Fig. 5.2 describes a schematic of this system. As depicted in Fig. 5.2, the RF thermal plasma system for the production of Ni nanoparticles mainly consists of an RF-ICP torch, an RF power supply with the plate power level of 200 kVA, a reactor, filtration and gas recycling system. Fig. 5.3 illustrates the cross-sectional view of an RF-ICP torch and a reactor, depicting flows of plasma gases, quenching gases, carrier gas, coolants and other processing gases. As shown in this figure, RF-ICP torch mainly comprises a four-turn induction coil and a ceramic confinement tube of 91 mm inner diameter. In addition, a vacuum tube oscillator was employed as a self-excited type RF power supply, performance data of which are summarized in Table 5.1. In this RF thermal plasma process, the mixture of argon and nitrogen was used as a plasma forming gas and the micron sized nickel powders (T123TM, >99.8%, Vale) were introduced into the RF thermal plasma as a precursor. In particular, nickel precursor was axially fed by helium carrier gas through a water-cooled injection port, which is located at the upper region of the induction coil.

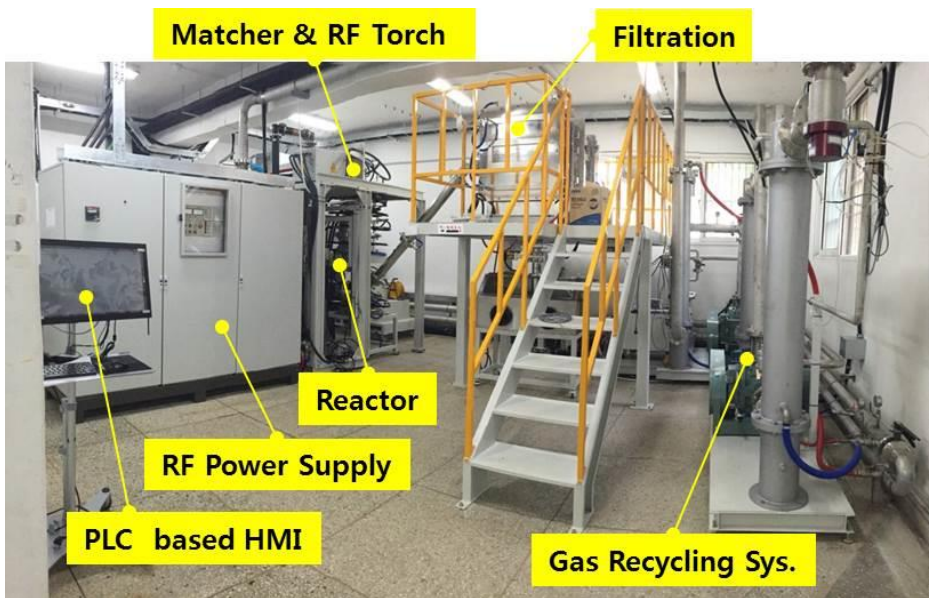


Figure 5. 1 A photograph of RF induction plasma system constructed.

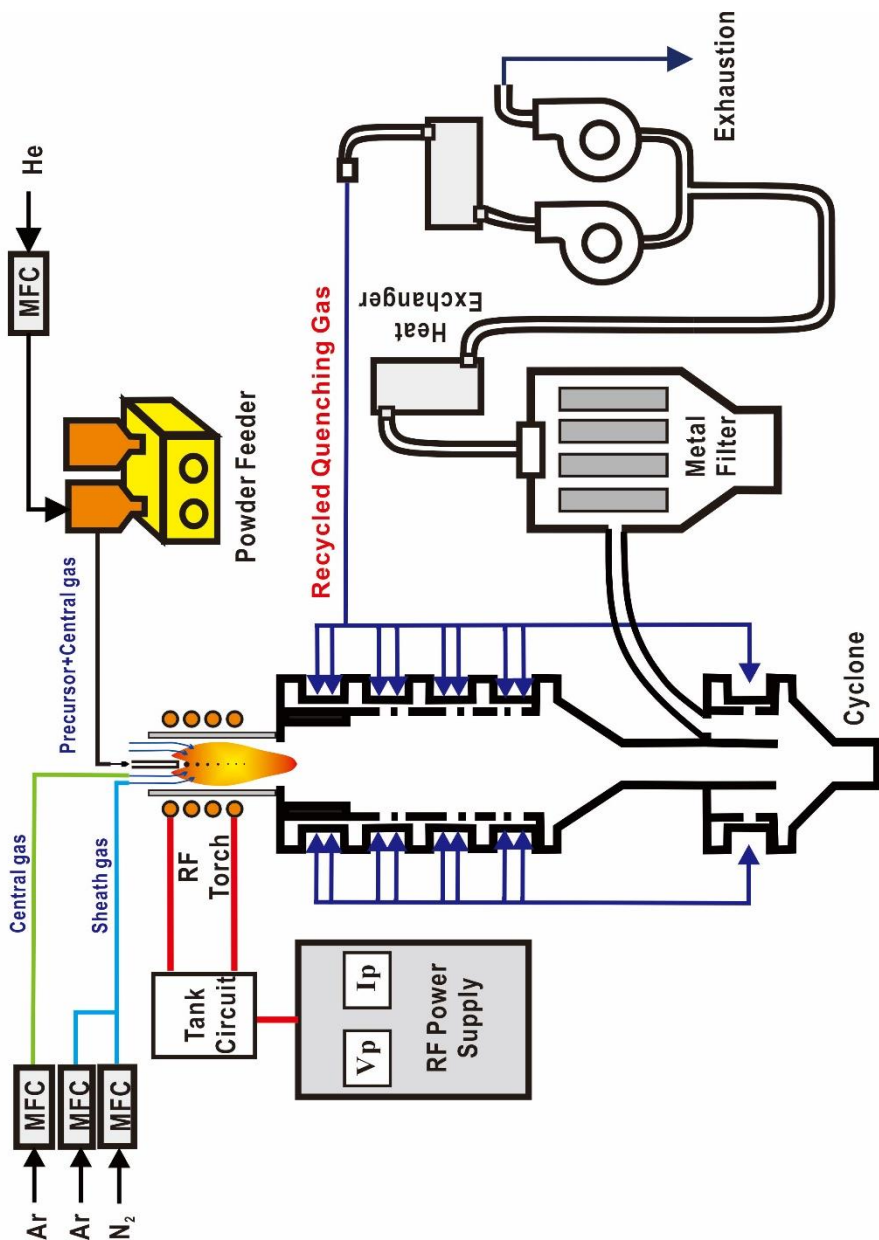


Figure 5. 2 Schematic of RF induction plasma system for the preparation of nanoparticles.

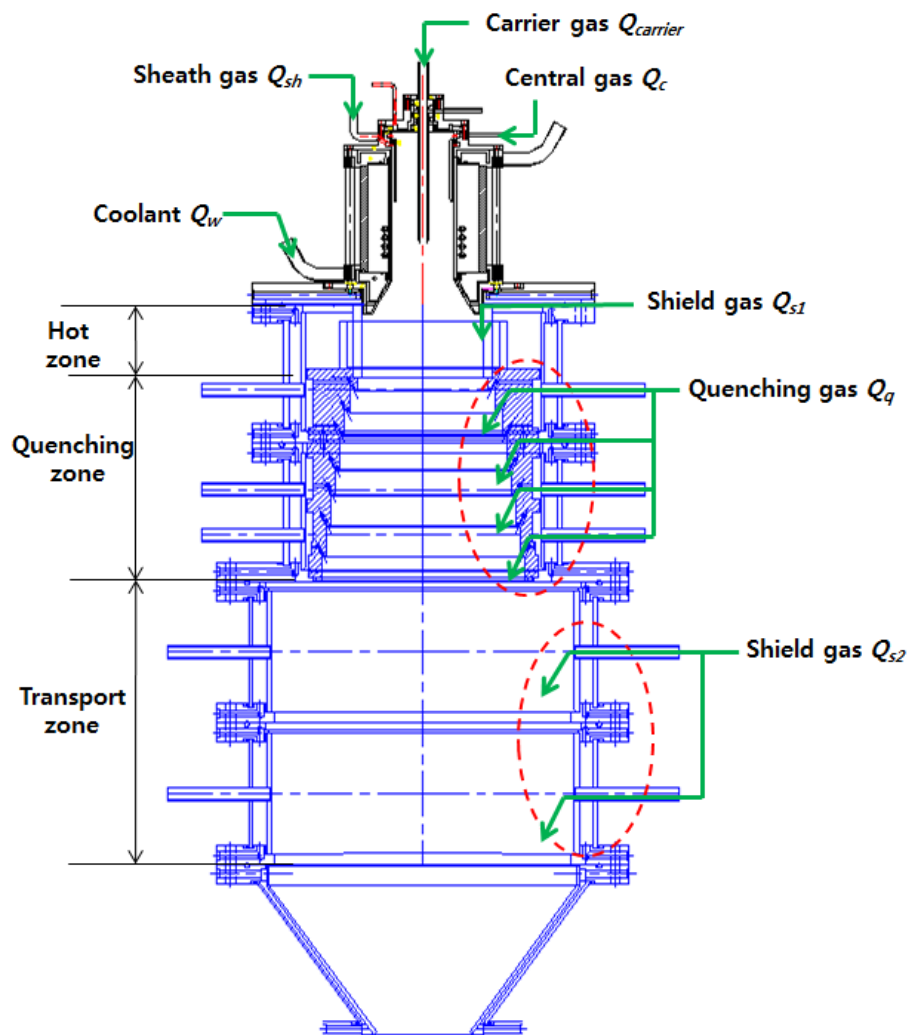


Figure 5. 3 A cross-sectional view of the RF ICP torch and reactor.

Table 5. 1 Specification of a self-excited type RF power supply with vacuum tube

Designation	Value
Intermediate circuit voltage DC	10.5 [kV]
Intermediate circuit current DC	19 [A]
Intermediate circuit power DC	200 [kW]
Output frequency	1 ~ 3 [MHz]
Output voltage	6600 [V]
Output Power	120 [kW]

Next, reaction chamber was designed to provide controllable reaction temperature and quenching zone suitable for the nucleation and growth of nickel nanoparticles. In the hot zone in Fig. 5.3, for example, graphite liners with 100 mm inner diameter were placed concentrically under the ICP torch exit to keep the high temperature region in the upper part of reactor. Then, the high temperature plasma flame is rapidly cooled down in the quenching zone by high flow rate quenching gas as shown in Fig. 5.3. In this zone, Ni vapors are expected to condense to solid particles and the particle sizes can be determined according to the nucleation and growth theory. After quenching zone, the as-prepared particles will be moved to the filtration through the successive transport zone as shown in Fig. 5.3. Table 5.2 lists up the principal design parameters and the operating conditions for the RF thermal plasma system used in this work. As summarized in Table 5.2, for example, the flow rates of plasma forming gas and quenching gas were kept at 200 slpm and 3500 slpm, respectively. The chamber pressure was controlled at 670 Torr and the plate power level of RF power supply is set at 80 kVA, which was estimated to correspond to RF input power of ~50 kW by calorimetric measurements of the

water coolants used to cool down the RF-ICP torch and RF power supply. In particular, the capacitance in tank circuit is determined by solving the equation (39) from the numerical results on the electrical characteristics in section 3.2. Fig. 5.4 shows the actual capacitors installed in impedance matching box, which consists of a tank circuit as an equivalent capacitance presented in Fig. 3.7



Figure 5. 4 A photograph of capacitors installed in impedance matching box, which consists of a tank circuit as an equivalent capacitance presented in Fig. 3.7

Table 5. 2 Principal design parameters and the operating conditions of RF induction plasma system for synthesis of Ni nanoparticles

Operating parameters			Value	Unit
Plate power			80	kVA
Carrier gas		(He)	5	slpm
Plasma gas	Central gas	(Ar)	50	slpm
	Sheath gas	(Ar)	110	slpm
	Sheath gas	(N ₂)	40	slpm
	N ₂ mole fraction		20	%
Carrier gas		(He)	5	slpm
Raw powder	Mean diameter		<10	µm
	Feed rate		20 ~ 40	g/min
Quenching gas		recycled	3500	slpm
Operating pressure			670	Torr
Design parameters			Value	Unit
Oscillating frequency			2~3	MHz
Number of coil turn			4	
Gap distance of coil			12.5	mm
Inner radius of injector			3.5	mm
Inner radius of confinement tube			45.5	mm
Turn radius of induction coil			56.25	mm

Finally, the as-synthesized nickel nano-powders were collected from the cyclone and the filter, respectively. They were observed by FE-SEM (Field Emission – Scanning Electron Microscopy) to check the sizes and shapes of particles. The crystallinity of the as-prepared powders was analyzed by XRD (X-ray diffraction). TGA (thermogravimetric analysis) was used to investigate the oxidation behavior of the as-prepared nickel nanopowders, i.e. the weight changes during their oxidation reaction in order to estimate the purity and the particle size distribution of them qualitatively.

5.2. Mass production of nickel nanoparticles by RF thermal plasma process

Figure 5.5 and 5.6 show the FE-SEM images of the micron-sized nickel precursor and the as-prepared nano-powders retrieved at filtration. In Fig. 5.5, Ni precursor is observed to have sizes of about 10 μm and irregular shapes. From the comparison between FE-SEM images in Figs. 5.5 and 5.6, it can be seen that micron-sized solid precursors are reformed into small particles with sizes under 200 nm (see Fig. 5.7 for size distribution of the as-prepared nanoparticles). In addition, the irregular shapes of Ni precursor are also transformed into spherical ones. From these electron microscopic observations, it can be concluded that the micron sized Ni powders in solid precursors underwent instantaneous evaporation during their passage of the RF thermal plasma flame, then, the produced vapors were condensed into very small particles with spherical shape as expected in RF thermal plasma process.

Figure 5.8 (a) and (b) presents FE-SEM images of the as-prepared particles collected from cyclone. As one can see in these figures, untreated or incompletely evaporated particles were dropped in cyclone due to their large sizes ($\sim 100 \mu\text{m}$). In addition, the sizes of the spherical particles collected from cyclone were increased compared with the sizes of precursor in Fig. 5.5. This formation of enlarged Ni ball indicates that there were many linkages and interactions between trajectories providing incomplete evaporation.

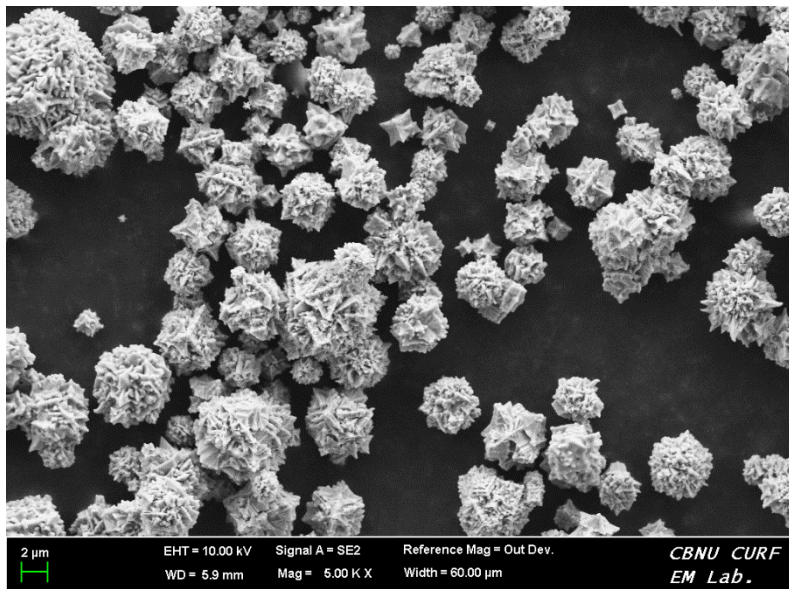


Figure 5. 5 SEM image of nickel raw powders.

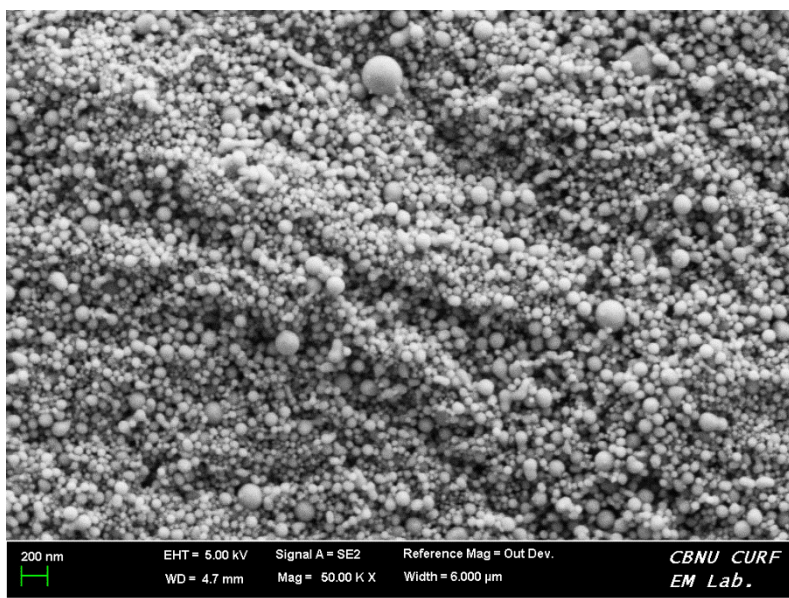


Figure 5. 6 SEM image of as-prepared nickel nanoparticles collected from filter.

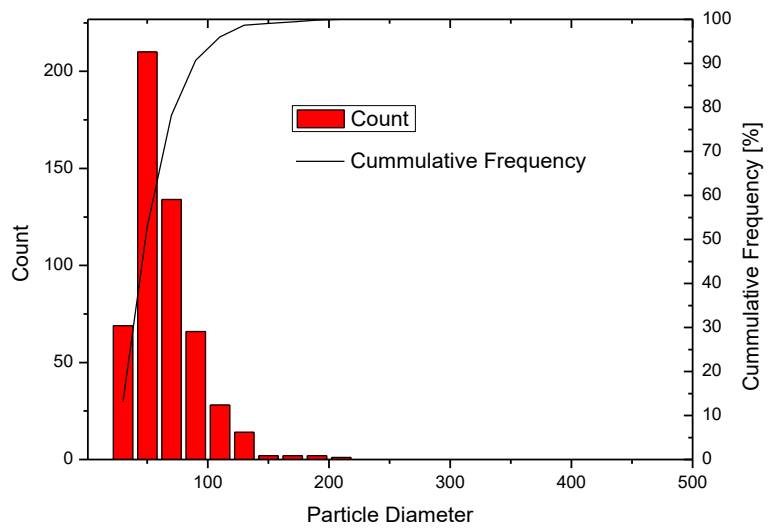


Figure 5. 7 Particle size distribution of the as-prepared nano-particles retrieved at filtration.

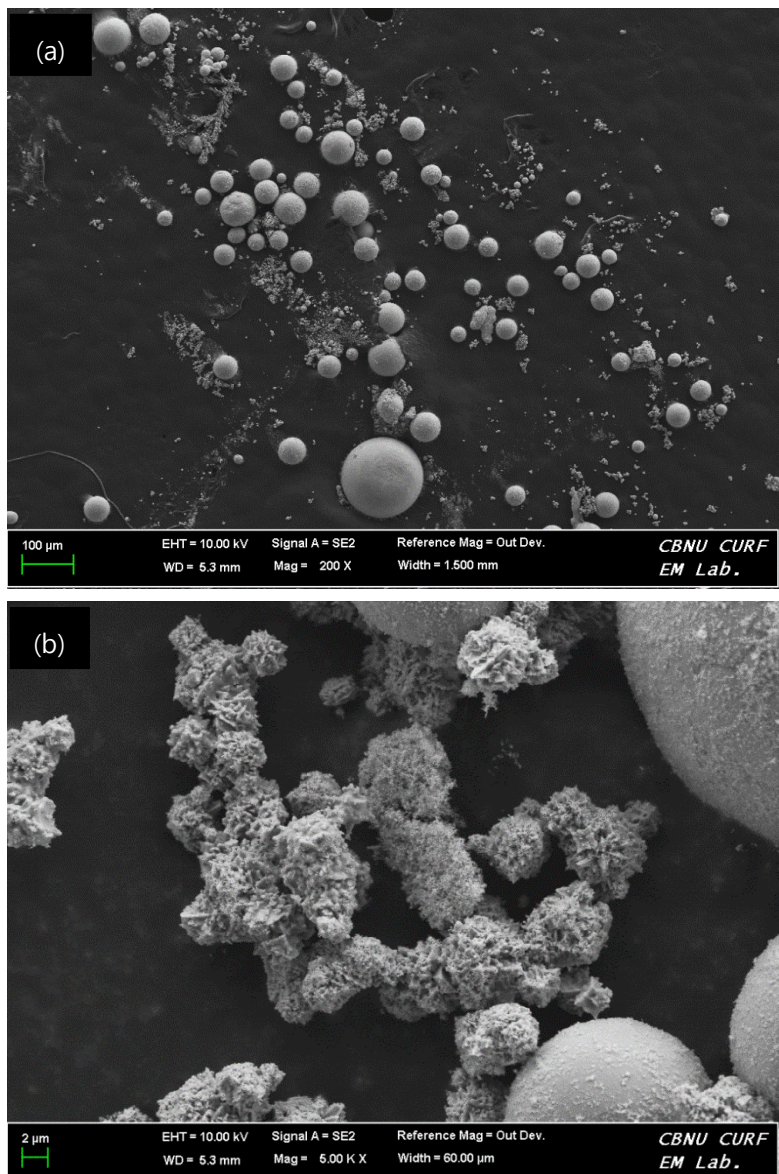


Figure 5. 8 FE-SEM images of the as-prepared particles collected from cyclone

Since these trajectories tend to be concentrated along the centerline as calculated in previous chapter, most of Ni ball in cyclone seems to result from Ni particles travelling along the centerline.

Fig. 5.9 presents the XRD data of the solid precursors and the as-prepared nano-powders retrieved at filtration. From the comparison between these XRD graphs, all of the crystalline peaks for Ni were observed with the small peaks for NiO in the as-prepared nano-powders. In spite of the size reduction and the transformation of spherical shape, these observation of crystalline peaks for Ni in the as-prepared nano-particles indicate that RF thermal plasma process is favorable for the synthesis of crystalline nano Ni powders with spherical shape thanks to its extremely high process temperatures as expected in Chapter 1. The peaks for NiO come from the passivation process after RF thermal plasma process of Ni precursor.

Fig. 5.10 shows TGA curves of nickel precursor and the as-prepared nanoparticles collected from filter. As can be seen in this figure, the as-prepared nanoparticles show slight reduction in weight between temperatures of 100 °C and 200 °C. This slight reduction in weight seems to be attribute to water in air reacted with nano Ni metal. Except this slight reduction in weight, the weight of the as-prepared nano-particles were kept constant, indicating relatively high purity of the as-prepared nano Ni particles. For the temperatures higher than 200 °C, however, the weight of the as-prepared nano-particles was rapidly increased as a result of oxidation, which also shows that most of the as-prepared nano particles were pure Ni metal.

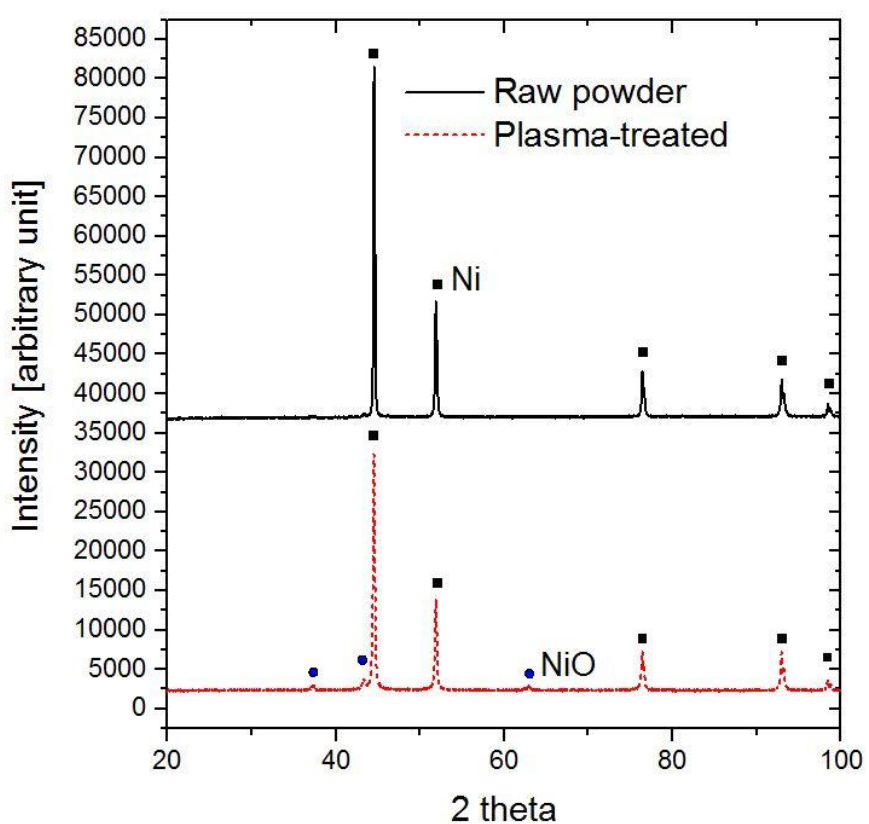


Figure 5. 9 XRD patterns of raw nickel powders and as-prepared nickel nanoparticles.

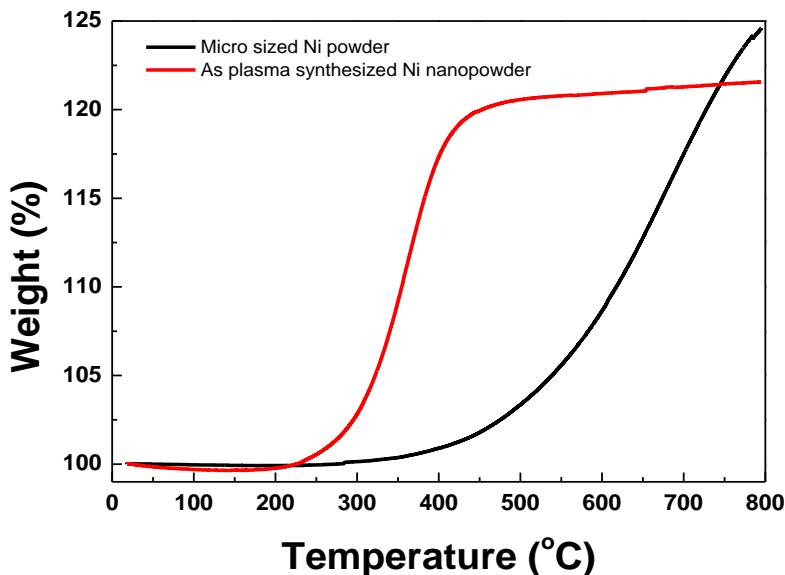


Figure 5. 10 TGA curves of nickel raw powder and as-prepared nickel nanoparticles collected from filter.

Finally, the yields of Ni powders retrieved at the filter and the cyclone were presented in Fig. 5.11 together with the evaporation ratio predicted from the numerical calculations as shown in Fig. 4.9. It should be noted that the two sets of data are not directly comparable. However, the experimental yields approximately follow the trend of change in the predicted evaporation ratios although the experimental results show lower values compared with the calculation result. These discrepancies originate from the wall deposition of nanoparticles, the differences of the operation pressure between the modelling and the experiment, and so on. This study experimentally verified the optimum conditions predicted numerically for mass production of Ni nanoparticles, such as RF power input of ~ 50 kW, N₂ content of 20 mol % and the feeding rate of ≥ 20 g/min.

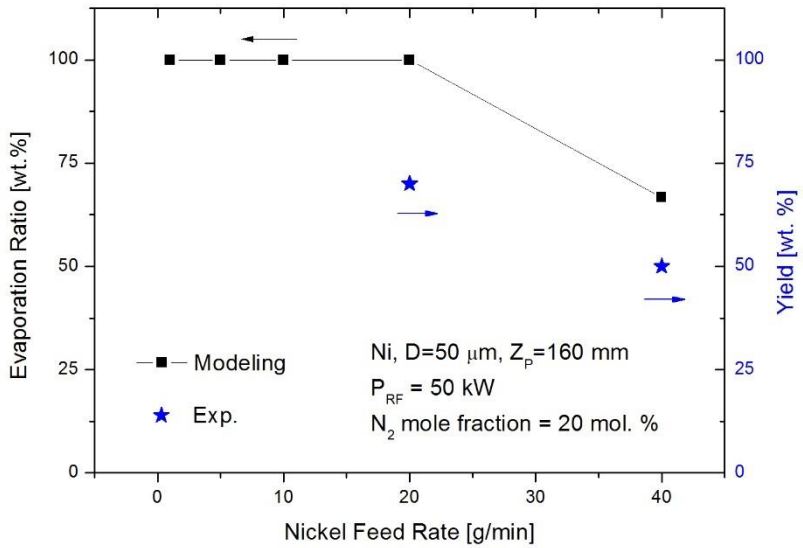


Figure 5. 11 Comparison between the yields of Ni nano-powders retrieved at filtration and the evaporation ratio predicted by numerical results

Chapter 6. Conclusions

In order to develop a practical RF induction thermal plasma process for the mass production of nickel nanoparticles and to understand the process, numerical and experiment study on RF induction plasma process is carried out.

A simplified PSI-Cell model is developed to consider the plasma-particle interaction with dense loading of raw nickel powders conditions for the mass production of nickel nanoparticles. To find out the optimal conditions of RF induction plasma process for the mass production of nickel nanoparticles, numerical simulations are conducted. From the computational study, effects of process parameters on the plasma characteristics and the behaviors of particles injected into induction torch are investigated.

Firstly, the effects of carrier gas flow on the flow fields of induction plasma and the behavior of a single particle injected into an induction torch are investigated. The introduction of cold carrier gas for powder feeding makes a low temperature zone downstream from the position of powder injection probe tip in the central region of RF induction torch. The low temperature zone expands and elongates with the increase of the carrier gas flow rate. As the carrier gas flow rate increases, the initial axial velocity of particle loaded in carrier gas flow is increased. Consequently, the residence time of particle in high temperature region decreases, which is disadvantageous to particle heat treatment. Therefore, the carrier gas flow rate should be minimized as much as possible for the complete evaporation of the powder injected.

Secondly, the effects of N₂ mole fraction of the plasma gas on the plasma characteristics and the behavior of particles injected into induction torch are studied. The addition of N₂ can reduce down the percentage of radiation power loss. The highest temperature region of ~ 10,000 K is significantly diminished

for Ar-N₂ induction plasma with the N₂ mole fraction of 20%, which is attributed to the increase of specific heat, enthalpy and thermal conductivity for N₂ addition. The Ar-N₂ mixture gas is also found to be advantageous to vaporize nickel particles due to the enhanced plasma-particle interaction.

Thirdly, the electrical characteristics of Ar-N₂ plasma were numerically analyzed according to N₂ content ranging from 0 mol% to 50 mol% at a plasma power level of 50 kW. From the computational results, the equivalent electrical resistance, R_{eq} is observed to decrease with the increase of N₂ mole fraction while equivalent electrical inductance, L_{eq} increases. The decrease of equivalent resistance, R_{eq} demonstrates that a greater coil current is required at the same power level in order to sustain Ar-N₂ RF-ICPs compared with Ar only RF-ICP. In addition, the behaviors of equivalent inductance, L_{eq} indicate that the electrical coupling efficiency can be deteriorated by N₂ addition. These results reveal that the tank circuit needs to be designed to compensate the changes in the impedance of Ar-N₂ RF-ICP for the scale-up of an RF-ICP system with a vacuum tube oscillator. Furthermore, the numerical model used in this work is expected to provide basic electrical data to determine the capacitance of a tank circuit as a design tool.

Fourthly, the effects of nickel feed rate on the temperature field of induction plasma and the behavior of particles injected into an induction torch are investigated. As the nickel feed rate increases, the plasma temperature drop near the particle trajectories increases due to the plasma-particle interaction. When the plasma is cooled down below the boiling point of nickel, plasma-particle heat transfer is reduced and the complete vaporization of the injected particles is difficult. The particles moving along with the outer trajectories far away from the symmetric axis of the torch can be completely vaporized because they pass through the high temperature region of induction plasma. However, the particles moving along with the inner trajectories close to the centerline of

the torch can be partly vaporized because they pass through the low temperature region of induction plasma.

Fifthly, the increase of RF power input affects two opposing effects. On the one hand, the increase of RF power input raises the plasma temperature, which has the favorable effects on the vaporization of the particles. On the other hand, the increase of RF power input increases the plasma axial velocity, which is disadvantageous to the vaporization of the particles. Consequently, the optimal RF power input to evaporate nickel powders is expected to exist.

In order to demonstrate the feasibility of the RF induction plasma process for the mass production of nickel nanoparticles, the RF induction plasma system for the preparation of nickel nanoparticles is constructed and the experimental work is carried out based on the computational study. Well-dispersed spherical nickel nanoparticles are successfully produced at an RF power input of 50 kW, 20 mol % of N₂ and a nickel feed rate of 20 g/min with the production yield of 65 wt. %. The mass production of Ni nanoparticles with spherical shape, high dispersion, high crystallinity and high purity is achieved via RF induction plasma process.

It is believed that the results of this work can be easily extended to the preparation of various nanoparticles on a large scale. In addition, the technical and scientific information obtained in this work on the features of thermal plasma process by using an RF induction plasma torch will be utilized to the various applications such as powder spheroidization and new material synthesis.

References

- [1] W. J. Tseng and C.-N. Chen, "Dispersion and rheology of nickel nanoparticle inks," *Journal of Material Science*, vol. 41, no. 4, pp. 1213-1219, 2006.
- [2] E. Antolini, M. Ferretti and S. Gemme, "Preparation of porous nickel electrodes for molten carbonate fuel cells by non-aqueous tape casting," *Journal of Materials Science*, vol. 31, no. 8, pp. 2187-2192, 1996.
- [3] J. R. Davis, Ed., Nickel, Cobalt, and Their Alloys, ASM international, 2000.
- [4] O. D. Neikov, S. S. Naboychenko and G. Dowson, Eds., Handbook of non-ferrous metal powders: technologies and applications, Elsevier, 2009.
- [5] H. Kishi, Y. Mizuno and H. Chazono, "Base-Metal Electrode-Multilayer Ceramic Capacitors: Past, Present and Future Perspectives," *Japanese Journal of Applied Physics*, vol. 42, no. 1, pp. 1-15, 2003.
- [6] J.-O. Hong, S.-H. Kim and K.-H. Hur, "Development History and Trend of High-Capacitance Multi-layer Ceramic Capacitor in Korea," *Journal of the Korean Ceramic Society*, vol. 46, no. 2, pp. 161-169, 2009.

- [7] J. Ding, T. Tsuzuki and P. G. McCormick, "Microstructural evolution of Ni-NaCl mixtures during mechanochemical reaction and mechanical milling," *Journal of Materials Science*, vol. 34, pp. 5293-5298, 1999.
- [8] C. Estournes, T. Lutz, J. Happich, T. Quaranta, P. Wissler and J. L. Guille, "Nickel nanoparticles in silica gel: preparation and magnetic properties," *Journal of Magnetism and Magnetic Materials*, vol. 173, pp. 82-92, 1997.
- [9] J. Gong, L. L. Wang, Y. Liu, J. H. Yang and Z. G. Zong, "Structural and magnetic properties of hcp and fcc Ni nanoparticles," *Journal of Alloys and Compounds*, vol. 457, no. 1, pp. 6-9, 2008.
- [10] S.-H. Wu and D.-H. Chen, "Synthesis and characterization of nickel nanoparticles by hydrazine reduction in ethylene glycol," *Journal of Colloid and Interface Science*, vol. 259, no. 2, pp. 282-286, 2003.
- [11] Z. G. Wu, M. Munoz and O. Montero, "The synthesis of nickel nanoparticles by hydrazine reduction," *Advanced Powder Technology*, vol. 21, no. 2, pp. 165-168, 2010.
- [12] K. H. Kim, H. C. Park, S. D. Lee, W. J. Hwa, S.-S. Hong, G.-D. Lee and S. S. Park, "Preparation of submicron nickel powders by microwave-assisted hydrothermal method," *Materials Chemistry and Physics*, vol. 92, no. 1, pp. 234-239, 2005.
- [13] T. Seto, K. Koga, H. Akinaga, F. Takano, K. Sakiyama, M. Hirasawa and T. Orii, "Laser synthesis and magnetic properties of monodispersed core-

- shell nanoparticles," *Applied Physics A*, vol. 79, no. 4-6, pp. 1165-1167, 2004.
- [14] J. L. H. Chau, "Synthesis of Ni and bimetallic FeNi nanopowders by microwave plasma method," *Materials Letters*, vol. 61, no. 13, pp. 2753-2756, 2007.
- [15] W.-N. Wang, Y. Itoh, I. W. Lenggoro and K. Okuyama, "Nickel and nickel oxide nanoparticles prepared from nickel nitrate hexahydrate by a low pressure spray pyrolysis," *Materials Science and Engineering B*, vol. 111, pp. 69-76, 2004.
- [16] J. GUO, X. FAN, R. DOLBEC, S. XUE, J. JUREWICZ and M. BOULOS, "Development of Nanopowder Synthesis Using Induction Plasma," *Plasma Science and Technology*, vol. 12, no. 2, pp. 188-199, 2010.
- [17] A. Tavakoli, M. Sohrabi and A. Kargari, "A Review of Methods for Synthesis of Nanostructured Metals with Emphasis on Iron Compounds," *Chemical Papers*, vol. 61, no. 3, pp. 151-170, 2007.
- [18] A. Umer, S. Naveed and N. Ramzan, "Selection of a suitable method for the synthesis of copper nanoparticles," *Nano*, vol. 7, no. 5, p. 1230005, 2012.
- [19] M. I. Boulos, "The inductively couple R.F. (radio frequency) plasma," *Pure and applied chemistry*, vol. 57, no. 9, pp. 1321-1352, 1985.

- [20] J.-H. Seo and B.-G. Hong, "Thermal plasma synthesis of nano-sized powders," *Nuclear Engineering and Technology*, vol. 44, no. 1, pp. 9-20, 2012.
- [21] S. L. Girshick, C.-P. Chiu, R. Muno, C. Y. Wu, L. Yang, S. K. Singh and P. H. McMurry, "Thermal Plasma Synthesis of Ultrafine Iron Particles," *Journal of Aerosol Science*, vol. 24, no. 3, pp. 367-382, 1993.
- [22] K. S. Kim, G. Cota-Sanchez, C. T. Kingston, M. Imris, B. Simard and G. Soucy, "Large-scale production of single-walled carbon nanotubes by induction thermal plasma," *Journal of Physics D: Applied Physics*, vol. 40, no. 8, p. 2375, 2007.
- [23] J. G. Li, M. Ikeda, R. Ye, Y. Moriyoshi and T. Ishigaki, "Control of particle size and phase formation of TiO₂ nanoparticles synthesized in RF induction plasma," *Journal of Physics D: Applied Physics*, vol. 40, no. 8, pp. 2348-2353, 2007.
- [24] G. Cota-Sanchez, G. Soucy, A. Huczko and H. Lange, "Induction plasma synthesis of fullerenes and nanotubes using carbon black-nickel particles," *Carbon*, vol. 43, no. 15, pp. 3153-3166, 2005.
- [25] M. Y. Lee, J. S. Kim and J. H. Seo, "Radio-frequency thermal plasma synthesis of nano-sized indium zinc tin oxide powders with reduced indium content," *Thin Solid Films*, vol. 521, pp. 60-64, 2012.
- [26] J. H. Seo, D. U. Kim, J. S. Nam, S. H. Hong, S. B. Sohn and S. M. Song, "Radio Frequency Thermal Treatment for Size Reduction and

Spheroidization of Glass Powders Used in Ceramic Electronic Devices," *Jounal of American Ceramic Society*, vol. 90, no. 6, pp. 1717-1722, 2007.

- [27] L. Bai, J. Fan, P. Hu, F. Yuan, J. Li and Q. Tang, "RF plasma synthesis of nickel nanopowders via hydrogen reduction of nickel hydroxide/carbonate," *Journal of Alloys and Compounds*, vol. 481, no. 1, pp. 563-567, 2009.
- [28] P. Proulx, J. Mostaghimi and M. I. Boulos, "Plasma-particle interaction effects in induction plasma modeling under dense loading conditions," *International Journal of Heat and Mass Transfer*, vol. 28, no. 7, pp. 1327-1336, 1985.
- [29] P. Proulx, J. Mostaghimi and M. I. Boulos, "Heating of Powders in an r.f. Inductively Coupled Plasma under Dense Loading Conditions," *Plasma Chemistry and Plasma Processing*, vol. 7, no. 1, pp. 29-52, 1987.
- [30] S. L. Girshick and W. Yu, "Radio-Frequency Induction Plasmas at Atmospheric Pressure: Mixtures of Hydrogen, Nitrogen, and Oxygen with Argon," *Plasma Chemistry and Plasma Processing*, vol. 10, no. 4, pp. 515-529, 1990.
- [31] S. V. Patankar, Computational Fluid Flow and Heat Transfer, New York: McGraw-Hill, 1980.
- [32] M. I. Boulos, "Heating of Powders in The Fire Ball of an Induction Plasma," *IEEE Transactions on Plasma Science*, Vols. PS-6, no. 2, pp. 93-106, 1978.

- [33] M. Rahmane, G. Soucy and M. I. Boulos, "Diffusion phenomena of a cold gas in a thermal plasma stream," *Plasma Chemistry and Plasma Processing*, vol. 16, Supplement 1, pp. S169-S189, 1995.
- [34] R. Ye, P. Proulx and M. I. Boulos, "Turbulence phenomena in the radio frequency induction plasma torch," *International journal of heat and mass transfer*, vol. 42, no. 9, pp. 1585-1595, 1999.
- [35] J. O. Hirschfelder, C. F. Curtiss and R. B. Bird, Molecular Theory of Gases and Liquids, 2nd ed., New York: Wiley, 1964.
- [36] S. Chapman and T. G. Cowling, The Mathematical Theory of Non-Uniform Gases, 3rd ed., Cambridge: Cambridge University Press, 1970.
- [37] A. B. Murphy, "Thermal plasmas in gas mixtures," *Journal of Physics D: Applied Physics*, vol. 34, no. 20, pp. R151-R173, 2001.
- [38] M. I. Boulos, P. Fauchais and E. Pfender, Thermal Plasmas, New York: Plenum Press, 1994.
- [39] A. B. Murphys and C. J. Arundell, "Transport Coefficients of Argon, Nitrogen, Oxygen, Argon-Nitrogen, and Argon-Oxygen Plasmas," *Plasma Chemistry and Plasma Processing*, vol. 14, no. 4, pp. 451-490, 1994.
- [40] J. Mostaghimi and M. I. Boulos, "Two-Dimensional Electromagnetic Field Effects in Induction Plasma Modelling," *Plasma Chemistry and Plasma Processing*, vol. 9, no. 1, pp. 25-44, 1989.

- [41] J. H. Park and S. H. Hong, "Optimization Analysis of an Inductively Coupled Plasma Torch for Material Processing by Using Local Thermal Equilibrium Numerical Models," *Journal of the Korean Physical Society*, vol. 31, no. 5, pp. 753-763, 1997.
- [42] J. H. Seo, J. M. Park and S. H. Hong, "Thermal Plasma Flow and Equivalent Circuit Analyses on the Electrical Coupling of a DC-RF Hybrid Plasma Torch," *Journal of the Korean Physical Society*, vol. 54, no. 1, pp. 94-104, 2009.
- [43] J. Kim, J. Mostaghimi and R. Iravani, "Performan Analysis of a Radio-Frequency Induction Plasma Generator Using Nonlinear State-Space Approach," *IEEE Transactions Plasma Science*, vol. 25, no. 5, pp. 1023-1028, 1997.
- [44] F. W. Grover, *Inductance Calculations*, New York: Van Nostrand, 1946.
- [45] C. T. Crowe, M. P. Sharma and D. E. Stock, "The Particle-Source-In Cell (PSI-CELL) Model for Gas-Droplet Flows," *Journal of Fluids Engineering*, vol. 99, no. 2, pp. 325-332, 1977.
- [46] S. Seely, *Radio electronics*, McGraw-Hill, 1956.

Appendix. Physical properties of Ar and N₂ plasmas

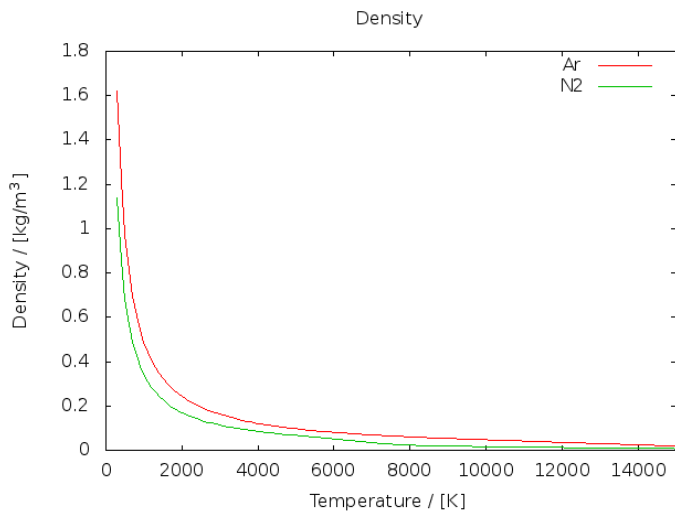


Figure A. 1 Density of Ar and N₂.

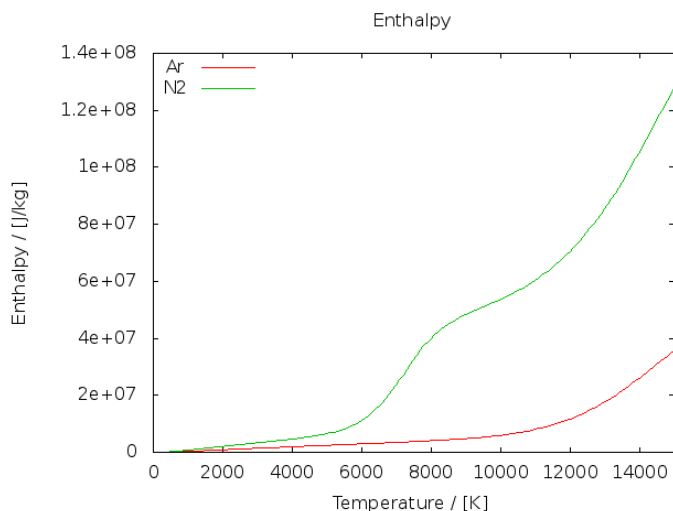


Figure A. 2 Enthalpy of Ar and N₂.

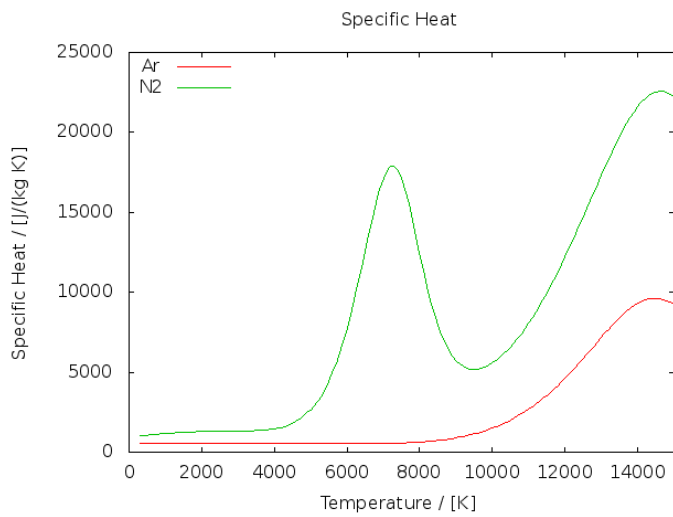


Figure A. 3 Specific heat of Ar and N₂.

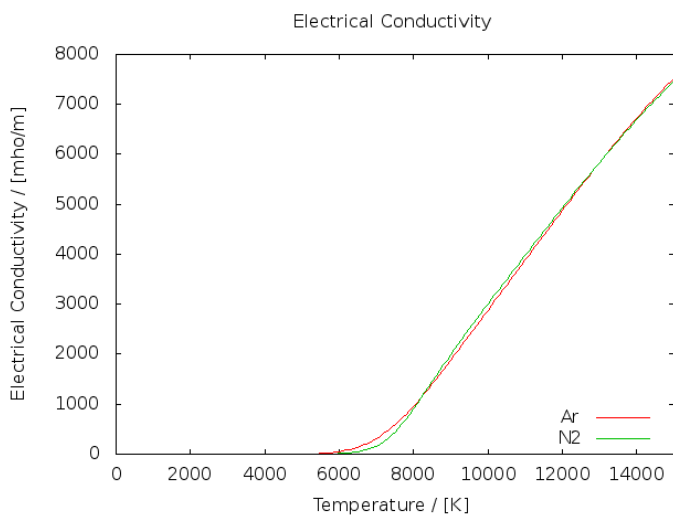


Figure A. 4 Electrical conductivity of Ar and N₂.

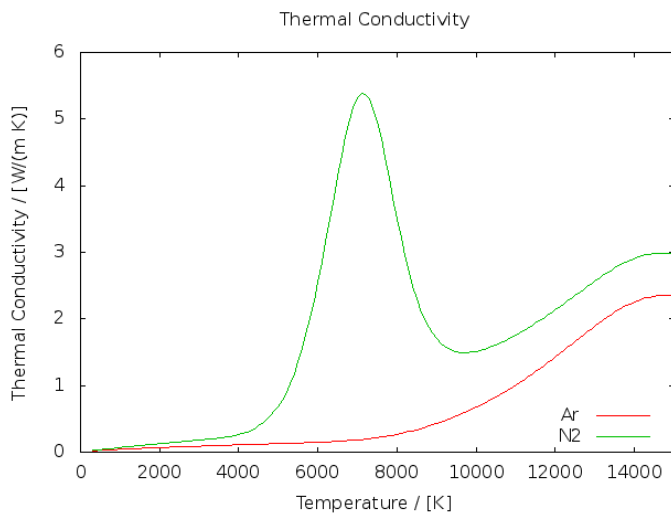


Figure A. 5 Thermal conductivity of Ar and N₂.

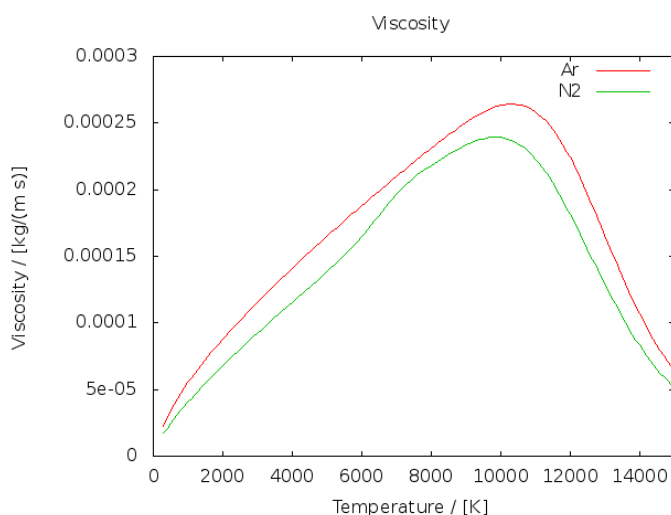


Figure A. 6 Viscosity of Ar and N₂.

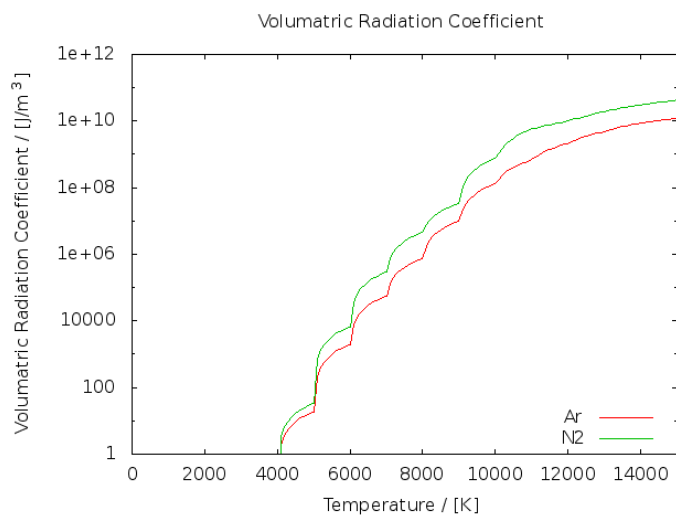


Figure A. 7 Volumetric radiation coefficient of Ar and N₂.

초록

최근 적층형 세라믹 캐패시터의 내부 전극 소재와 같은 니켈 나노입자의 수요 증가와 함께 경제적인 니켈 나노입자 합성법 개발의 필요성이 커지고 있다. 특히 적층형 세라믹 캐패시터의 내부 전극 용 니켈 나노입자는 그 형상이 구형이어야 하며, 고순도, 좁은 입도분포, 우수한 분산성과 고결정성의 높은 품질이 요구된다. 그러나 볼밀법, 졸겔법과 같은 종래의 나노입자 합성법들은 이러한 품질 기준을 만족시키기 어렵거나 대량 생산이 힘들어 산업적 응용에 한계가 있다. 반면에 고주파 유도결합 열플라즈마 공정을 이용한 나노입자의 제조는 재래식 방법에 비해서 분산성이 우수한 구형 나노입자의 제조에 강점을 보여 큰 관심을 받고 있다. 그러나 상업화 측면에서는 공정 효율 개선과 운전비용 절감이 요구되고 있다. 본 연구에서는 나노입자의 대량생산화를 통해 이러한 단점을 개선하고자 하였다.

본 학위연구의 목적은 니켈 나노입자의 대량생산을 위한 고주파 유도결합 열플라즈마 제조 공정의 개발에 있다. 니켈 나노입자의 대량생산을 위해서는 먼저 원료가 되는 니켈 분말의 대량 주입($\geq 1.0 \text{ kg/h} = 16.7 \text{ g/min}$)이 가능해야 한다. 그리고 주입된 분말의 기화율을 높이기 위한 고출력 운전 조건을 찾아야 한다. 이를 위해 수치해석과 실험에 의한 공정 해석 연구를 수행하였다.

원료의 대량 투입에 따른 플라즈마-입자 상호작용을 모사하기 위한 수치해석 코드를 개발하였다. 수치해석을 통해 공정 변수가

플라즈마 유동과 플라즈마에 주입된 니켈 입자의 기화율에 미치는 영향을 살펴보았다.

첫째, 이송기체의 도입은 원료 주입구의 하류에 저온 영역을 형성시킨다. 이송기체 유량이 증가할수록 저온 영역의 길이가 증가하며, 이송 기체에 실려 이송되는 입자의 속도도 증가한다. 따라서 입자가 고온 영역에 머무는 시간도 감소하여 플라즈마-입자 사이의 열전달이 감소하는 것으로 해석되었다.

둘째, 알곤-질소 혼합 기체의 질소 함량에 따른 플라즈마의 전기적 특성 변화와 고주파 토치에 대한 등가회로 해석을 수행하였다. 질소 함량이 늘수록 플라즈마 등가 저항은 감소하고 플라즈마 등가 인덕턴스는 증가하는 경향을 보였다. 이로부터 질소 함량이 늘수록 동일한 플라즈마 출력에 대해 보다 큰 전류를 필요로 하며, 이를 위해서는 탱크회로의 정전용량을 증가시켜야 함을 알 수 있었다.

셋째, 알곤-질소 혼합 기체의 사용은 니켈 입자의 대량 처리를 위한 고출력 고주파 열플라즈마 발생에 유리할 뿐만 아니라, 플라즈마의 열용량과 열전도도 향상을 통해서 플라즈마-입자 사이의 열전달을 향상시켜 대량 입자 처리에 유리함을 밝혔다.

넷째, 단위 시간당 니켈 투입량을 증가시키면 플라즈마-입자 상호작용에 따라 입자가 이동하는 궤적 인근의 플라즈마 온도가 감소한다. 토치 중심축에서 멀리 떨어진 고온 영역을 이동하는 입자는 완전 기화가 가능하나, 중심축에 가까운 궤적을 따라 저온 영역을 이동하는 입자는 표면의 일부만 기화하거나 원형을 유지하며 지나갈 것으로 예상되었다.

다섯째, 고주파 전력은 플라즈마를 가열하여 온도를 증가시키므로 플라즈마-입자 사이의 열전달을 증가시켜 입자 기화에 유리한 영향을 미치지만, 동시에 플라즈마의 축방향 유속을 증가시켜 입자의 체류시간을 감소시키므로 입자 기화에 불리한 영향을 미친다. 따라서 고주파 전력의 최적값이 존재하는 것으로 분석되었다.

수치해석 결과를 바탕으로, 실험 장치를 구성하고, 제안된 범위에서 니켈 나노입자 제조실험을 수행하였다. 고주파 입력 전력 50 kW, 질소 몰 분율 20%, 단위 시간당 니켈 투입량 20 g/min에 대해 약 65 wt. %의 수율로 평균 100 nm 이하의 잘 분산된 구형의 니켈 나노입자를 얻을 수 있었다.

이상의 연구 결과들은 나노입자 제조를 위한 고주파 열플라즈마 공정에 대한 이해를 높여 여러 산업 분야에서 요구되는 다양한 종류의 나노입자에 대한 경제적인 대량생산 기술 개발에 확대 적용될 수 있을 것으로 기대된다. 또한 본 연구를 통해 개발된 고주파 유도결합 열플라즈마 수치해석 기법과 공정에 대한 정보는 고주파 열플라즈마를 이용한 입자 구형화, 표면 코팅, 신물질 합성과 같은 다양한 분야에 응용될 수 있을 것이다.

주요어: 고주파 열플라즈마, 고주파 유도결합 플라즈마, 플라즈마-입자 상호작용, 나노입자 합성, 니켈, 수치해석

학번: 2004-30210